

# Honey, I Shrunk the Arc de Triomphe!

Yuanbo Xiangli<sup>1,2</sup>, Hanyu Chen<sup>1</sup>, Xueqing Tsang<sup>1</sup>, and Noah Snavely<sup>1</sup>

<sup>1</sup> Cornell University

<sup>2</sup> Shanghai Jiao Tong University

**Abstract.** Metric scale monocular geometry estimation has seen significant progress through large-scale data aggregation, yet current foundation models suffer from a persistent “scale-collapse” phenomenon: distant landmarks and vast landscapes are metrically underestimated. This performance gap stems from a training data bottleneck, where existing metric-scale datasets are hardware-constrained to unvaried street-level LiDAR or short-range indoor scans, or consist of synthetic data that lacks the semantic complexity of the physical world. To bridge this gap, we curate a new metrically-grounded, in-the-wild dataset that we call *MetricScenes*, gathered from a variety of sources including Internet photo collections and stereo imagery. We estimate camera poses and initial depth maps for each scene using off-the-shelf methods, and recover absolute scale from geo-tagged metadata as well as known stereo camera baselines. We also improve the quality of depth maps derived from MetricScenes via a new two-stage Poisson completion method. Fine-tuning MoGe-2 on our dataset significantly mitigates scale-collapse and achieves superior metric accuracy in unconstrained, open-domain scenes while maintaining state-of-the-art performance on standard benchmarks. Project page: <https://metricscenes.github.io/>.

**Keywords:** In-the-wild metric-scale dataset · Monocular metric geometry · Monocular metric depth

## 1 Introduction

Determining absolute scene scale from a single image is an inherently ill-posed task. Consider the tourist photo of the Arc de Triomphe in Fig. 1. From visual information alone, we can’t be completely certain that we’re looking at the monumental real-world landmark, as opposed to a cleverly constructed toy scene. However, there are visual cues to absolute scale, some of which humans rely on, such as reference objects of known scale (*e.g.*, people). Modern monocular geometry estimation (MGE) models ought to be able to perform a similar deduction via such semantic priors and other cues.

However, we found that current state-of-the-art methods frequently fail to estimate correct scene scale, leading to a persistent *scale-collapse* phenomenon in “in-the-wild” scenarios. Fig. 1 shows an example where clear semantic references (people) are present, yet where models like MoGe-2 [33] exhibit a significant scale

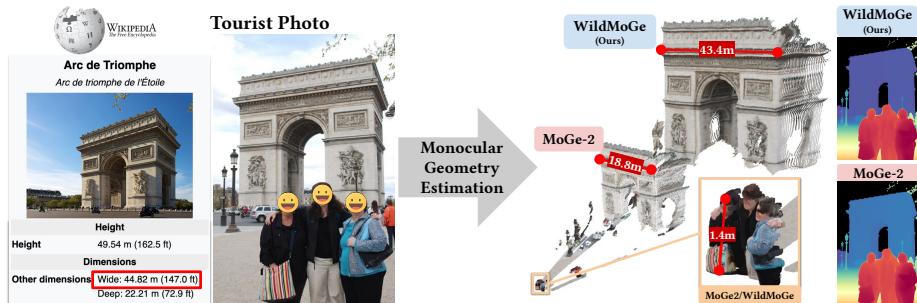


**Fig. 1: Scale-collapse in metric geometry estimation.** State-of-the-art monocular geometry estimation (MGE) methods like MoGe-2 [33] exhibit a persistent scale-collapse phenomenon, where far-field structures are metrically shrunk and pulled toward the camera. According to Wikipedia, the real Arc de Triomphe has a physical width of 44.8 m, but MoGe-2 predicts a metric point cloud of width just 18.8 m. By fine-tuning on our proposed MetricScenes dataset, our model, WildMoGe, recovers a more faithful landmark scale (43.4 m) while maintaining consistent metric estimation for foreground subjects ( $\sim 1.4$  m).

inconsistency across the range of distances: the predicted metric scale for near-field objects is plausible—in this case, the tourists have a plausible height—yet the scale for far-field structures is dramatically underestimated—here, the Arc de Triomphe in the background is metrically predicted to be just 18.8 m wide, which is more than  $2\times$  smaller than the ground truth width (44.8 m). MoGe-2 has posited a miniaturized landmark, despite cues to the contrary.

We argue that this performance gap is due to limitations in available training data. Current metric-scale, real-world datasets are restricted to two narrow categories due to hardware constraints: 1) terrestrial LiDAR datasets like KITTI [30] and Argoverse 2 [38], which are predominantly confined to vehicle-mounted street scenarios featuring limited diversity, and 2) active 3D scanner-captured data, such as ScanNet++ [43] and ARKitScenes [1], which are restricted by their short effective range to small-scale environments like indoor rooms. Synthetic datasets attempt to bridge this gap through diverse perspectives and motions [4, 8, 34], but fail to capture the true metric diversity of the real world due to the reliance on procedural rules and limited 3D assets.

To enrich the availability of real-world metric data, we introduce *MetricScenes*, a large-scale dataset curated from a variety of commonplace visual sources including Internet photo collections and stereo imagery. These sources provide the environmental and semantic variety missing from existing hardware-constrained datasets. We reconstruct camera viewpoints and initial depth maps via off-the-shelf methods, then recover absolute physical scale by leveraging geolocated landmark metadata and stereo camera baselines. Specifically, we aggregate data from AerialMegaDepth [32], MegaScenes [29], and Stereo4D [11], and develop pipelines to extract metric-scale depth maps in each case. We observe that depth maps derived from SfM and MVS often lack foreground transients. Naive Poisson completion fails here because the gradient guidance produced by monocular models also suffer from *scale-collapse*, causing the solver to

unnaturally enlarge foreground objects or distort boundaries. To remedy this, we propose a two-stage edge-aware Poisson completion algorithm that decouples background metric alignment from foreground integration, ensuring sharp boundaries and consistent metric scale throughout the view. We show that fine-tuning MoGe-2 on MetricScenes significantly improves metric accuracy for unconstrained, in-the-wild photos. Our model generalizes effectively to novel scenes while maintaining performance comparable to state-of-the-art methods on standard benchmarks.

## 2 Related Work

**Scale Ambiguity.** Recovering absolute dimensions from a single image involves inherent scale ambiguity. Despite advances, resolving true physical scale remains a central challenge for monocular metric depth and geometry estimation (MDE/MGE). Early works like ZoeDepth [2] and LeRes [45] attempted to bridge this gap using domain-specific metric heads or focal length decoupling. Recent foundation models have introduced more sophisticated alignment strategies. The Metric3D series [10,44] transform images into a virtual camera space to resolve metric ambiguity across diverse data sources. UniDepth v2 [23] employs a self-prompting camera module, which simultaneously learns to predict camera embeddings. MoGe-2 [33] decouples structural geometry from global scale, utilizing DINOv2 global tokens for scale prediction.

However, these architectural innovations are often insufficient for robust “in-the-wild” generalization. As shown in Fig. 1, state-of-the-art models suffer from scale-collapse in unconstrained environments, often underestimating the dimensions of distant structures. This performance gap suggests that the primary bottleneck is no longer architectural, but rather a fundamental lack of scale-diverse, real-world training data.

**Metric-scale Datasets.** Real-world metric depth datasets relied on physical sensors like terrestrial LiDAR (*e.g.*, KITTI [30], Argoverse 2 [38], Waymo [28]) and active 3D scanners (*e.g.*, ScanNet++ [43], ARKitScenes [1]). While scale-accurate, these are restricted to driving corridors with limited diversity or small-scale indoor rooms and often suffer from spatial misalignment and sensor asynchrony. To bypass these hardware limits, synthetic datasets, like urban-focused MatrixCity [17] and Synscapes [39], indoor-oriented Hypersim [24], and aerial-view TartanAir [34], provide noise-free, dense labels across diverse domains. To further improve generalization, internet-scale collections like MegaDepth [19] and BlendedMVS [42] use structure from motion methods [25] to reconstruct scenes with wide semantic diversity, though they recover geometry only up to an unknown scale.

We analyzed standard training data and found a critical imbalance: large-scale in-the-wild SfM datasets offer semantic variety but lack metric scale. Metric supervision is currently split between LiDAR-based datasets, comprising 59% of outdoor metric frames but limited to driving scenarios; and the rest are

synthetic data, which lacks real-world complexity. No existing large-scale real-world dataset simultaneously provides absolute scale and in-the-wild diversity. Our work addresses this gap by creating MetricScenes, a real-world metric-scale dataset that provides depth training data that is both metric and sharp.

### 3 Generating Metric-Scale 3D Data

To fill critical gaps and add diversity missing in existing real-world metric datasets, we leverage widely available visual sources, including Internet photo collections and stereo imagery. In Sec. 3.1, we describe how we process noisy Internet photo collections and recover physical scale using geo-tagged metadata. In Sec. 3.2, we cover how we acquire high-quality dense depth maps from stereo video sequences and recover metric scale using known camera baselines. The initial depth maps we obtain from off-the-shelf vision methods often contain holes and missing regions. In Sec. 3.3, we describe a new two-stage edge-aware depth completion strategy that preserves correct scene scale and geometry while enhancing depth sharpness.

#### 3.1 Internet Photo Collections

We gather imagery from AerialMegaDepth [32] and MegaScenes [29], which consist of diverse Internet-sourced photography, including historical archives, tourist snapshots, and professional imagery. Specifically, AerialMegaDepth enhances MegaDepth [19] by jointly reconstructing landmarks with geo-tagged aerial views rendered from Google Earth. MegaScenes provides a vast collection of SfM reconstructions recovered at an arbitrary scale. We leverage geo-tagged images from online mapping services to anchor these reconstructions to absolute physical dimensions.

**Robust SfM and MVS.** For AerialMegaDepth, we use the SfM results provided in their dataset. For MegaScenes, we implement a pipeline addressing both structural errors and local depth inaccuracies. First, to resolve potential Doppelgänger issues [5], where visually similar but geographically distant 3D surfaces cause spurious correspondences that mislead the reconstruction, we follow [40] to obtain sparse reconstruction results with MAST3R-SfM [7] and the Doppelgänger classifier. For both AerialMegaDepth and MegaScenes, after MVS [26], on the obtained geometric depths, we apply a stability filtering strategy to identify and remove unstable pixels with high depth variance, and leverage MoGe-2’s predictions to filter out depth-bleeding regions where background depth eats away foreground depth [18, 19]. This depth refinement pipeline ensures the final labels are geometrically consistent and free from dynamic artifacts. Examples are shown in Fig. 2.

**Metric-Scale Recovery from Geolocations.** To establish a globally consistent metric coordinate system, we leverage geo-referenced imagery to anchor

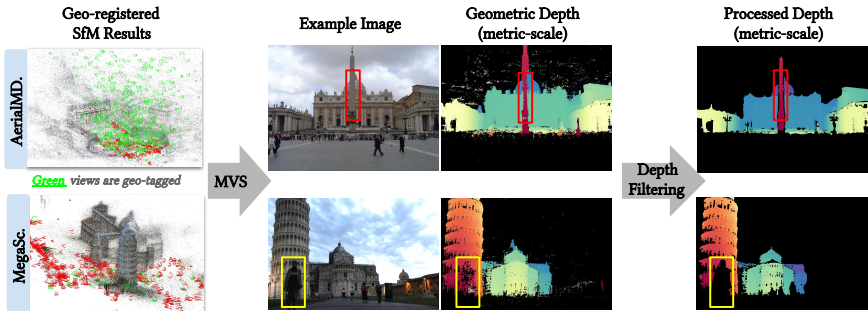


**Fig. 2: Metric depth from Internet photo collections.** Geo-tagged images obtained from online mapping sites like Google Earth/Google Street View can be used to scale SfM results to absolute metric scale. AerialMegaDepth [32] is reconstructed with pseudo-synthetic views rendered from Google Earth and scenes are scaled accordingly. MegaScenes [29] contains natively unscaled SfM results. We augment these SfM models with georeferenced street-level views to scale the geometry to physical dimensions. After scaling and running MVS, we apply a depth filtering method to remove transient objects (yellow box) and filter out depth-bleeding regions (red box).

our 3D reconstructions, as illustrated in Fig. 2. AerialMegaDepth achieves metric scale by jointly reconstructing Internet photos with Google Earth renderings from specified, geolocated viewpoints. Since the rendered viewpoints are inherently metrically grounded, the resulting models inherit the absolute metric scale. Since MegaScenes lacks metric information, we leverage online mapping sites (e.g. Google Street View<sup>3</sup>) to obtain geo-tagged street view images:

- **Viewpoint sampling:** We ascertain the landmark’s outline and sample approximately 100 evenly distributed viewpoints along surrounding roads.
- **Coverage optimization:** To ensure full-facade coverage, we query for images with camera headings directed toward the scene center and apply geometric occlusion checks to remove obstructed views.
- **Data preference:** We prioritize imagery and metadata contributed by professional providers over those from individual users, as the former offers more accurate geolocation.

To register these geo-tagged images to existing reconstructed SfM models in MegaScenes, we use a method based on MAST3R. Specifically, MAST3R descriptors are used to compute matches between geo-tagged images and the existing reconstructed models. To resolve matching ambiguities arising from scene symmetries or repetitive elements, we use the Doppelganger classifier [40] to prune spurious correspondences in the scene graph. After registering the geo-tagged images, we use the COLMAP’s model aligner [25] to rotate the reconstruction into a Manhattan World frame, ensuring the dominant vertical and horizontal structures in the scenes are axis-aligned. To establish absolute metric scale and positioning, we apply RANSAC to robustly estimate a similarity transformation between the recovered 3D camera positions and their corresponding

<sup>3</sup> <https://developers.google.com/maps/documentation/streetview/overview>

Earth-Centered, Earth-Fixed (ECEF) coordinates. To ensure robustness, we discard scenes with implausible scale factors, high mean registration errors, or low RANSAC inlier ratios.

### 3.2 Stereo Imagery

The Stereo4D dataset [11] provides a large-scale collection of diverse, real-world stereoscopic video sequences captured using VR180 devices. The dataset originally offers roughly-estimated metric scaled depth maps, using the assumption that most VR180 stereo cameras have a baseline of approximately 6.3 cm (optimizing for the average human interpupillary distance). However, we observed that in practice, the physical baseline varies between different camera rigs. To ensure precise metric recovery, we utilize a subset of Stereo4D videos where camera configurations are explicitly documented in the video description.

**Robust Multi-View Reconstruction.** Stereo4D originally relies on an optical flow estimator, SEA-RAFT [36], to derive scene geometry. However, we find that imperfect stereo calibration often causes both optical flow and dedicated stereo matching algorithms (e.g., FoundationStereo [37]) to produce unreliable results. As illustrated in Fig. 3, the recovered geometry exhibits severe surface distortion, where parallel building facades unnaturally converge toward a distant point.

Therefore, to generate more reliable depth maps, we propose to use a *multi-view reconstruction* pipeline that re-estimates camera calibration, poses, and depth. For each video clip in Stereo4D, we first sample a target center frame and extract  $N = 16$  surrounding frames with a temporal stride of  $K = 3$ . This spacing ensures sufficient temporal context and prevents the inclusion of many near-duplicate frames. Rather than relying on per-frame two-view stereo, we pass all  $N + 1$  stereo pairs to a multi-view reconstruction model to jointly estimate camera poses and scene geometry. This approach leverages broader spatio-temporal context, leading to more accurate and consistent depth estimates than single-pair methods. We evaluated several methods, including  $\pi^3$  [35], DepthAnything V3 [20] and MapAnything [13], and ultimately selected  $\pi^3$  due to its geometric robustness and ability to recover sharp local details (see Fig. 3).

**Metric-Scale Recovery from Camera Baselines.** Since  $\pi^3$  produces reconstructions in an arbitrary coordinate frame, we recover the absolute metric scale for each scene by aligning the average predicted baseline between the reconstructed stereo pairs to the known physical baseline. Specifically, denoting the physical baseline of the stereo rig as  $b_{\text{gt}}$ , we compute a global scale factor  $s$  as:

$$s = \frac{b_{\text{gt}}}{\frac{1}{N+1} \sum_{i=0}^N \|\mathbf{t}_{\text{L}}^{(i)} - \mathbf{t}_{\text{R}}^{(i)}\|_2}, \quad (1)$$

where  $\mathbf{t}_{\text{L}}^{(i)}$  and  $\mathbf{t}_{\text{R}}^{(i)}$  are the estimated translation vectors of the left and right cameras for the  $i$ -th sampled frame. Raw depth values  $d_{\text{pred}}$  are then scaled to produce the final metric depths:  $d_{\text{metric}} = s \cdot d_{\text{pred}}$ .

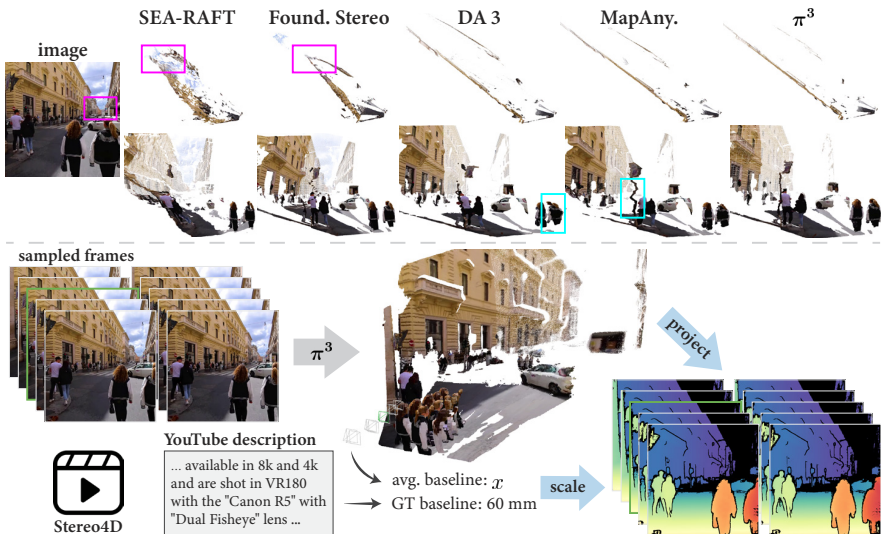


**Fig. 3: Metric Depth from Stereo4D [11].** Top: Standard stereo matching [36,37] often produces distorted geometry in poorly calibrated in-the-wild videos, as seen in the converging facades (magenta boxes). Among multi-view models [13,20,35],  $\pi^3$  [35] maintains the most robust geometry and sharp local details (cyan boxes). Bottom: We process stereoscopic sequences via  $\pi^3$  to obtain dense geometry and poses, then compute a global scale factor to align the predicted baseline with the camera’s physical baseline. This yields accurately scaled metric depth maps.

**Frame Sampling and Filtering.** Since frames within a clip are highly similar, we sample one sequence per clip and include only a single frame from the sequence in the final dataset to maximize dataset diversity. Specifically, we choose the *center-left frame* in the sequence as it benefits from the most bidirectional temporal context during the multi-view reconstruction process. To ensure high quality training data, we filter the target frame according to several criteria:

- **Image quality:** We discard underexposed frames based on their median intensity. Additionally, we filter out motion-blurred frames that lack sufficient high-frequency detail based on their Tenengrad gradient energy.
- **Geometric consistency:** To ensure geometric accuracy, we perform a depth reprojection check on the stereo pair and discard the frame if more than 10% of valid pixels are depth-inconsistent between the two views.
- **Calibration accuracy:** We reject frames violating expected stereo constraints. A frame is discarded if the inferred baseline deviates from the physical baseline by more than 10 mm (after scaling via Eq. 1) or if the relative camera rotation exceeds  $1^\circ$ .

To ensure reliable supervision from these pseudo-labels, we compute a robust scale factor between the derived metric depth from previous steps and the MoGe-2 prediction. If this factor exceeds  $2\times$  or falls below  $0.5\times$ , we discard the frame as the scale is likely unreliable. This filtering is justified because  $\pi^3$  consistently

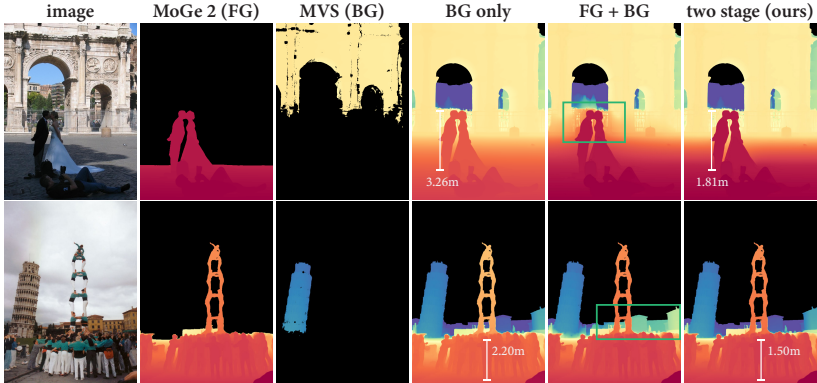


**Fig. 4: Visual comparison of depth completion methods.** With gradient guidance from MoGe-2, using only background anchors (BG only) preserves structure but uniformly mis-scales the entire map, yielding an implausible foreground (e.g., a 3.26m tall person). Combining foreground and background anchors in a single stage (FG+BG) forces the solver to reconcile conflicting scales, causing depth bleeding and scale drift (green boxes). Our two-stage approach maintains accurate metric scale for both foreground and background while ensuring sharp, artifact-free boundaries.

recovers near-field geometry (e.g. pedestrians close to camera, nearby buildings as in Fig. 3), a domain where MoGe-2 typically demonstrates high reliability.

### 3.3 Depth Fusion and Completion

Depth maps from prior stages are typically incomplete: Internet photos lack foregrounds and transient objects (Fig. 2), while stereo imagery lacks backgrounds due to low confidence on distant points (Fig. 3). Conversely, monocular models predict dense, continuous geometry but have problematic metric scale estimation. As a result, these sources become complementary: our processed depth maps provide sparse metric anchors for scale, while monocular predictions offer structural guidance to fill holes and refine edges. Fusing them should produce depth maps that are both metrically accurate and visually complete.

**Single-Pass Geometry Completion.** To reconstruct missing depth, MoGe-2 introduced a *logarithmic-space Poisson completion* strategy. Their original approach integrates the incomplete ground truth depth map with guidance from a monocular depth model trained exclusively on synthetic data. Specifically, this is achieved by minimizing the gradient differences in the log domain:

$$\min \sum_{i \in \Omega} \|\nabla(\log d_i^*) - \nabla(\log \hat{d}_i)\|^2, \quad \text{s.t.} \quad d_i^* = d_i, \quad \forall i \in \partial\Omega, \quad (2)$$

where  $d_i^*$  is the solved depth,  $\hat{d}_i$  is the predicted depth providing gradient guidance, and  $d_i$  represent fixed ground truth anchors bordering missing regions.

We found that this strategy effectively completes Stereo4D depth maps but faces a critical limitation on AerialMegaDepth and MegaScenes due to the scale-collapse phenomenon. Specifically, MoGe-2 often predicts an incorrect scale for

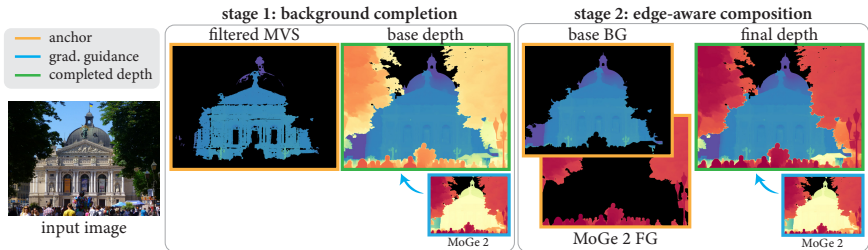


**Fig. 5: Overview of the two-stage depth completion pipeline.** Stage 1 performs a Poisson solve using the gradient guidance of MoGe-2’s depth map, constrained by the filtered MVS results. This yields a base depth map with an accurate background scale, though the foreground exhibits scale-drift. In Stage 2, the background isolated from the base depth map (base BG) and the MoGe-2 foreground (MoGe-2 FG) serve as joint anchors for the final completion. We perform an edge-weighted Poisson solve using these anchors, reusing MoGe-2’s gradient guidance to produce a globally consistent metric depth map with sharp local details.

distant landmarks, while maintaining a plausible scale for foreground subjects (Fig. 1). Because the Poisson solver treats the depth map as a continuous field, a scale correction forced by background anchors propagates globally through these gradient constraints. This results in a proportionate expansion of foreground objects, *e.g.* the physically impossible 3.26 m tall person in Fig. 4 (BG only), making foreground scale unreliable.

To resolve this scale conflict, we propose anchoring the Poisson completion by trusting MoGe-2 to recover the metric scale of foreground content while relying on filtered MVS results for the absolute scale of background regions. A naive solution would be to adapt Eq. 2 to use both the MVS background and MoGe-2 foreground as fixed anchors. However, this approach fails because the solver is still forced to reconcile conflicting scales across the entire scene. As shown in Fig. 4 (FG+BG), unanchored transition regions such as a building’s base are inevitably warped toward the foreground to satisfy global gradient constraints.

**Two-stage Edge-Aware Completion.** We attribute geometric distortion in single-stage solves to anchor sparsity, which provides insufficient constraints to override the scale-collapse inherent in the gradients of MoGe-2’s depth prediction. Without a dense reference, the solver cannot reconcile the sparse metric anchors with a gradient field that pulls the background forward. This forces transition regions to warp as the geometry ‘stretches’ to satisfy collapsed gradients between the fixed foreground and background metric anchors. To address this, we propose a two-stage completion pipeline:

- **Stage 1: Background Completion.** We first apply Eq. 2 using only sparse background depth as anchors, yielding results like in Fig. 4 (BG only). In this stage, the background is reconstructed at a consistent metric scale without being warped by foreground depth constraints. We then discard the incorrectly scaled foreground regions, retaining only the completed background for the subsequent stage.

- **Stage 2: Edge-Aware Composition.** We combine the completed background from Stage 1 with the MoGe-2 predicted foreground to form a composite anchor. To preserve sharp boundaries and prevent depth-bleeding artifacts, the second Poisson solve utilizes an *edge-weighted* objective:

$$\min \sum_{i \in \Omega} \sum_{j \in \mathcal{N}(i)} w_{ij} \|(\log d_i^* - \log d_j^*) - (\log \hat{d}_i - \log \hat{d}_j)\|^2, \quad (3)$$

where the weight  $w_{ij}$  approaches zero across sharp depth discontinuities.

Example results are shown in Fig. 4 (last column). Because the background is now densely anchored by the Stage 1 output, it remains fixed to its correct metric scale, while the edge weights ensure the foreground is integrated with crisp, artifact-free boundaries. Our full pipeline is illustrated in Fig. 5.

## 4 Evaluation

### 4.1 Dataset Overview

The MetricScenes dataset contains 47,579 images from 134 scenes in Aerial-MegaDepth (only real-world images), 29,583 images across 356 scenes from MegaScenes, and 22,549 frames from 1,725 videos<sup>4</sup> in Stereo4D. This diverse collection provides extensive coverage across a variety of perspectives and environments, including ground-level and aerial views, urban and natural landscapes, and both indoor and outdoor settings. We reserve a held-out set of 10 scenes from AerialMegaDepth, 10 scenes from MegaScenes, and 10 videos from Stereo4D to serve as validation and test sets.

### 4.2 WildMoGe

We fine-tune the MoGe-2 ViT-Large-Normal model on our MetricScenes dataset for 10,000 iterations with a batch size of 32 (approximately 3 epochs), ensuring model convergence while preventing significant divergence from the pre-trained geometric priors. We adopt the image cropping and data augmentation strategies from the original MoGe-2 implementation. We use a learning rate of  $1 \times 10^{-6}$  for the backbone and  $1 \times 10^{-5}$  for the remaining parameters. Further details can be found in the supplemental material.

### 4.3 Qualitative Results

In this section, we compare depth reconstructions of novel in-the-wild scenes obtained by our fine-tuned model, WildMoGe, as well as (vanilla) MoGe-2 [33], DepthAnything v3 [20], Metric3D v2 [10], UniDepth v2 [23], and DepthPro [3]. These results are visualized in Fig. 6. Additionally, we provide a comparison between WildMoGe and MoGe-2 on scenes prevalent in the standard training datasets, with results shown in Fig. 7.

<sup>4</sup> There are 1,725 videos, separated into 22,549 clips, and we sample 1 frame per clip.



**Fig. 6: Metrology of novel in-the-wild scenes.** The first column shows images with measurements obtained via Google Map’s measuring tool. We merge WildMoGe and MoGe-2’s results into a single column to highlight the accurate scaling achieved by our training scheme. WildMoGe consistently recovers more accurate absolute scales across diverse landmarks, whereas MoGe-2 [33], DepthAnything v3 [20] and Metric3D v2 [10] exhibit scale-collapse, underestimating the scale of background structures. While Unidepth v2 [23] produces more realistic scales, they still deviate from ground truth. DepthPro [3] often produces scales orders of magnitude smaller than reality.

From Fig. 6, we observe that WildMoGe consistently recovers more accurate absolute scales across diverse landmarks, closely matching ground-truth dimensions (*e.g.*, 31.4m vs. 32.4m for the Philadelphia Museum of Art, 46.7m vs 46.5m for Piazza della Signoria). MoGe-2, DepthAnything v3 and Metric3D v2 [5] exhibit scale-collapse behavior, consistently underestimating the size of far-field structures. UniDepth v2 produces more realistic scales but still deviates from ground truth, and DepthPro often fails to recover absolute scale, producing results that are orders of magnitude smaller than reality. Note that these scenes are absent from the training set. This performance demonstrates that WildMoGe can generalize to unseen content, as opposed to simply memorizing training scenes.

Fig. 7 demonstrates that WildMoGe provides scale estimates consistent with MoGe-2 in common indoor and street environments. For instance, both models estimate a door height of 2.1m and a car length of approximately 3.2m to 3.3m. However, on the ETH3D [27] courtyard scene, WildMoGe recovers a more accurate, smaller scale than MoGe-2. Specifically, WildMoGe estimates a desk

<sup>5</sup> Metric3D v2 struggles with plausible sky depth, measurements in Fig. 6 are taken on the building facades, not the sky artifacts.

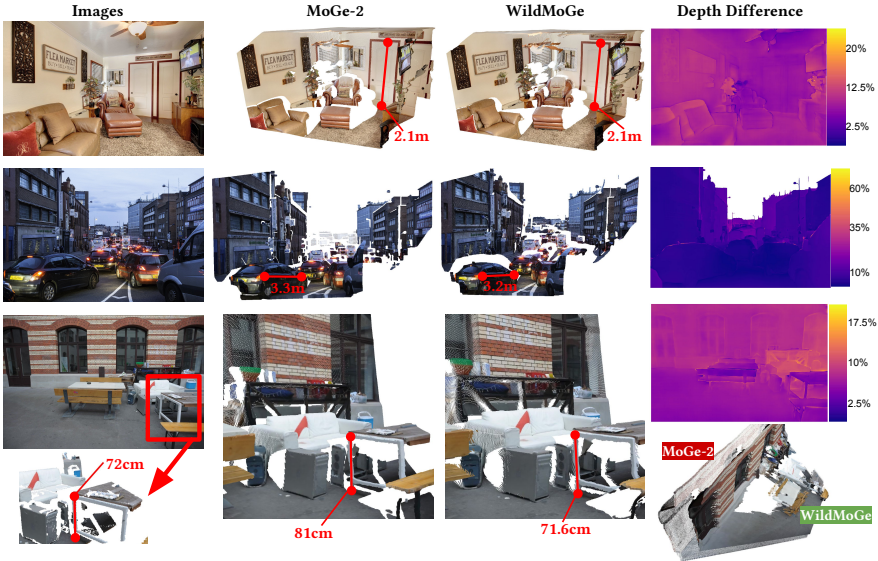


**Fig. 7: Comparison on the standard scenes.** We compare WildMoGe against MoGe-2 [33] on representative indoor and street-level scenes. In standard indoor and street contexts (Rows 1 & 2), WildMoGe provides scale estimates consistent with MoGe-2. On the ETH3D [27] courtyard scene (Row 3), WildMoGe achieves better accuracy, recovering a desk leg height of 71.6cm compared to the 72cm ground truth. This implies that WildMoGe’s performance is driven by precise metric grounding rather than a bias toward larger scales.

leg height of 71.6cm, closely matching the 72cm ground truth, whereas MoGe-2 overestimates it at 81cm. This indicates that WildMoGe is *not* merely biased toward predicting larger scales as in Fig. 1 & 6, but is instead performing reliable estimation grounded in absolute metric geometry.

#### 4.4 Quantitative Evaluation

Obtaining precise and dense ground-truth data for unconstrained, in-the-wild scenes is inherently challenging. Therefore, we provide quantitative results on our curated test set while acknowledging that these results may be less definitive due to potential imperfections in the test set labels. To provide a more comprehensive assessment, we also conduct evaluations on the standard benchmarks to demonstrate that our model is comparable to state-of-the-art performance in specialized environments while effectively bridging the gap between hardware-constrained training data and unconstrained, in-the-wild scenarios.

**Benchmark.** For the MetricScenes test set, we treat the partial dense depth maps generated *before* the Poisson completion step (Sec. 3.3) as our ground truth. For Internet photo collections, these labels are filtered geometric depth maps from MVS that have been metrically scaled using geo-tagged metadata (Sec. 3.1). For stereo imagery, the labels are from  $\pi^3$  multi-view reconstruction

**Table 1: Quantitative evaluation of relative and metric geometry.** The top section evaluates on the standard benchmarks, while the bottom section evaluates on MetricScenes test set. Metrics are color-coded: **red** (best) and **yellow** (second best).

| Method                                     | Relative Geometry             |   |                    |                               |                               |   |                                       | Metric Geometry                 |                               |                                 |                               |                                |                               |             |             |             |
|--|-------------------------------|---|--------------------|-------------------------------|-------------------------------|---|---------------------------------------|---------------------------------|-------------------------------|---------------------------------|-------------------------------|--------------------------------|-------------------------------|-------------|-------------|-------------|
|  | Point                         |   | Local              |                               | Depth                         |   |                                       | Point                           |                               | Depth                           |                               |                                |                               |             |             |             |
|  | Scale-inv. Rel <sup>d</sup> ↓ | Affine-inv. δ <sub>1</sub> <sup>p</sup> ↑ | Rel <sup>d</sup> ↓ | δ <sub>1</sub> <sup>p</sup> ↑ | Scale-inv. Rel <sup>d</sup> ↓ | Affine-inv. δ <sub>1</sub> <sup>d</sup> ↑ | Affine-inv. (disp) Rel <sup>d</sup> ↓ | (w/o GT Cam) Rel <sup>d</sup> ↓ | δ <sub>1</sub> <sup>p</sup> ↑ | (w/o GT Cam) Rel <sup>d</sup> ↓ | δ <sub>1</sub> <sup>d</sup> ↑ | (w/ GT Cam) Rel <sup>d</sup> ↓ | δ <sub>1</sub> <sup>d</sup> ↑ |             |             |             |
| <i>Evaluation on standard benchmarks</i>   |                               |   |                    |                               |                               |   |                                       |                                 |                               |                                 |                               |                                |                               |             |             |             |
| ZoeDepth                                   | -                             | -   | -                  | -                             | 12.7                          | 83.9                                      | 10.1                                  | 88.5                            | 11.1                          | 88.3                            | -                             | -                              | 39.3                          | 49.9        | -           | -           |
| Metric3D V2                                | -                             | -   | -                  | -                             | 7.92                          | <b>91.8</b>                               | 7.66                                  | 92.9                            | 9.51                          | 89.4                            | -                             | -                              | -                             | -           | 18.3        | 73.9        |
| DA V2                                      | -                             | -   | -                  | -                             | 10.7                          | 87.6                                      | 8.48                                  | 90.8                            | 8.82                          | 91.6                            | -                             | -                              | 29.9                          | 56.6        | -           | -           |
| DA V3                                      | 12.0                          | 86.5                                      | 9.42               | 88.9                          | 7.18                          | 93.4                                      | 8.99                                  | 89.4                            | 7.40                          | 91.8                            | 8.63                          | 91.4                           | 9.71                          | 89.3        | 18.0        | 67.7        |
| MASt3R                                     | 14.5                          | 82.1                                      | 11.6               | 86.0                          | 8.09                          | 92.2                                      | 11.2                                  | 86.5                            | 9.38                          | 89.1                            | 11.6                          | 87.8                           | 26.2                          | 55.3        | 49.7        | 30.3        |
| UniDepth V2                                | 11.6                          | 87.7                                      | 8.56               | 91.9                          | 6.34                          | 94.9                                      | 8.61                                  | 90.8                            | 6.42                          | 93.9                            | 7.35                          | 93.0                           | 10.1                          | 91.9        | 21.3        | <b>75.3</b> |
| Depth Pro                                  | 12.4                          | 87.7                                      | 9.93               | 89.4                          | 6.91                          | 94.1                                      | 9.81                                  | 89.1                            | 7.65                          | 92.0                            | 8.42                          | 91.7                           | 13.7                          | 81.9        | 27.6        | 54.4        |
| MoGe-2                                     | <b>10.8</b>                   | <b>88.5</b>                               | <b>7.98</b>        | <b>91.7</b>                   | <b>5.33</b>                   | <b>95.9</b>                               | <b>7.35</b>                           | <b>92.2</b>                     | <b>5.62</b>                   | <b>94.8</b>                     | <b>6.66</b>                   | <b>93.8</b>                    | <b>8.19</b>                   | <b>93.6</b> | <b>15.7</b> | <b>76.8</b> |
| WildMoGe                                   | 10.1                          | 89.3                                      | 7.68               | 92.2                          | 5.50                          | 95.8                                      | 7.49                                  | 91.8                            | 5.63                          | 94.7                            | 6.97                          | 93.7                           | 8.39                          | 93.1        | 15.6        | 73.4        |
| <i>Evaluation on MetricScenes test set</i> |                               |   |                    |                               |                               |   |                                       |                                 |                               |                                 |                               |                                |                               |             |             |             |
| MoGe-2                                     | 6.76                          | 95.0                                      | 4.56               | 96.9                          | -                             | -   | 4.85                                  | 95.4                            | 3.42                          | 97.4                            | 4.61                          | 96.3                           | 11.7                          | 87.3        | 37.2        | 37.7        |
| WildMoGe                                   | 5.24                          | 97.0                                      | 3.67               | 97.9                          | -                             | -   | 4.02                                  | 97.1                            | 2.98                          | 98.2                            | 4.15                          | 97.1                           | 7.59                          | 93.4        | 26.5        | 73.8        |

results scaled by camera baselines (Sec. 3.2). We also follow MoGe-2 [33] to evaluate the accuracy of our model on 10 standard datasets: NYUv2 [22], KITTI [30], ETH3D [27], iBims-1 [14, 15], GSO [6], Sintel [4], DDAD [9], DIODE [31], Spring [21], and HAMMER [12].

**Baselines.** We compare our method to MoGe-2 [33], UniDepth V2 [23], Depth Pro [3], MASt3R [16], Depth Anything V2 [41] & V3 [20], ZoeDepth [2] and Metric3D V2 [10].

**Relative Geometry and Depth.** Following MoGe-2, we evaluate relative geometry to assess how effectively each method reconstructs scene structure from a single input image. We measure performance across multiple representations, including scale-invariant and affine-invariant point maps, local point maps within each detected objects, and scale-invariant depth, as well as affine-invariant depth and disparity. Specifically, the relative error for point maps is defined as  $Rel^p = \|\hat{\mathbf{p}} - \mathbf{p}\|_2 / \|\mathbf{p}\|_2$  and for depth maps as  $Rel^d = |\hat{z} - z|/z$ . We also report the percentage of inliers using the thresholds  $\delta_1^p = (\|\hat{\mathbf{p}} - \mathbf{p}\|_2 / \|\mathbf{p}\|_2 < 0.25)$  and  $\delta_1^d = \max(\hat{d}/d, d/\hat{d}) < 1.25$  across the 10 evaluation datasets. ZoeDepth, DepthAnything V2, and Metric3D V2 are excluded from the point-based evaluations as these models do not provide camera intrinsic predictions. On the MetricScenes test set, we omit local point map evaluation because our ground truth depth maps can be sparse. Tab. 1 (left side) presents quantitative results on relative geometry and depth prediction. On the standard benchmarks, our WildMoGe achieves performance comparable to MoGe-2 while outperforming all other baselines. On the MetricScenes test set, WildMoGe consistently surpasses MoGe-2 across all metrics. This indicates that fine-tuning on MetricScenes does not severely compromise the model’s existing geometric priors; instead, it bridges the gap between near-field and far-field scale estimation on in-the-wild scenes, allowing the model to generalize effectively to unconstrained environments.

**Metric Geometry and Depth.** We evaluate the accuracy of metric-scale geometry and depth across seven datasets with metric-scale annotations: NYUv2 [22], KITTI [30], ETH3D [27], iBims-1 [14, 15], DDAD [9], DIODE [31], and HAMMER [12]. We report relative point error ( $Rel^p$ ) and percentage of inliers ( $\delta_1^p$ ) on predicted metric point maps. Similarly, we evaluate metric depth accuracy

**Table 2: Ablation of finetuning MoGe-2 using different subsets of MetricScenes.** Evaluation is conducted on the standard benchmarks and MetricScenes’s test set. We evaluate performance across relative geometry, metric geometry, and boundary sharpness. Metrics are color-coded: **red** (best) and **yellow** (second best). Boundary sharpness is reported on a subset of the standard benchmarks [4, 12, 15, 21], but is omitted for the MetricScenes test set.

| Method                                     | Relative Geometry   |                   |                     |                   |                     |                    |                     |                   |                     |                   | Metric Geometry     |                   |                     |                   | Sharpness           |                |      |      |      |
|--|---------------------|-------------------|---------------------|-------------------|---------------------|--------------------|---------------------|-------------------|---------------------|-------------------|---------------------|-------------------|---------------------|-------------------|---------------------|----------------|------|------|------|
|  | Point               |                   |                     |                   |                     | Depth              |                     |                   |                     |                   | Point               |                   | Depth               |                   | Boundary            |                |      |      |      |
|  | Scale-inv.          | Affine-inv.       | Local               | Scale-inv.        | Affine-inv.         | Affine-inv. (disp) | (w/o GT Cam)        | (w/o GT Cam)      | (w/ GT Cam)         | (w/ GT Cam)       | $F_1 \uparrow$      |                   |                     |                   |                     |                |      |      |      |
| $RelP \downarrow$                          | $\delta P \uparrow$ | $RelP \downarrow$ | $\delta P \uparrow$ | $RelP \downarrow$ | $\delta P \uparrow$ | $RelD \downarrow$  | $\delta D \uparrow$ | $RelD \downarrow$ | $\delta D \uparrow$ | $RelD \downarrow$ | $\delta D \uparrow$ | $RelD \downarrow$ | $\delta D \uparrow$ | $RelD \downarrow$ | $\delta D \uparrow$ | $F_1 \uparrow$ |      |      |      |
| <i>Evaluated on the standard Benchmark</i> |                     |                   |                     |                   |                     |                    |                     |                   |                     |                   |                     |                   |                     |                   |                     |                |      |      |      |
| All  | 10.1                | 89.3              | 7.68                | 92.2              | 5.50                | 95.8               | 7.49                | 91.8              | 5.63                | 94.7              | 6.97                | 93.7              | 8.39                | 93.1              | 15.6                | 73.4           | 13.5 | 84.9 | 15.5 |
| Stereo4D only                              | 11.3                | 88.0              | 8.00                | 91.8              | 5.52                | 95.8               | 7.50                | 92.3              | 5.65                | 94.8              | 6.77                | 93.7              | 9.29                | 91.4              | 19.0                | 63.4           | 15.0 | 82.2 | 15.6 |
| AerialMD. only                             | 9.81                | 90.2              | 7.39                | 92.9              | 5.59                | 95.7               | 7.41                | 92.6              | 5.65                | 94.9              | 6.70                | 93.8              | 8.60                | 93.4              | 16.8                | 78.9           | 14.6 | 85.8 | 14.5 |
| MegaSc. only                               | 9.78                | 90.2              | 7.32                | 92.8              | 5.45                | 95.8               | 7.45                | 91.9              | 5.51                | 95.0              | 6.75                | 93.9              | 8.68                | 91.5              | 15.9                | 73.0           | 13.7 | 82.5 | 15.0 |
| AerialMD.+MegaSc.                          | 9.73                | 90.6              | 7.33                | 92.1              | 5.52                | 95.7               | 7.40                | 92.1              | 5.52                | 94.9              | 6.69                | 93.9              | 8.36                | 92.5              | 16.0                | 74.2           | 13.2 | 85.1 | 14.9 |
| <i>Evaluated on MetricScenes Test Set</i>  |                     |                   |                     |                   |                     |                    |                     |                   |                     |                   |                     |                   |                     |                   |                     |                |      |      |      |
| All  | 5.24                | 97.0              | 3.67                | 97.9              | -                   | -                  | 4.02                | 97.1              | 2.98                | 98.2              | 4.15                | 97.1              | 7.59                | 93.4              | 26.5                | 73.8           | 26.0 | 79.1 | -    |
| Stereo4D only                              | 6.23                | 96.6              | 3.83                | 97.6              | -                   | -                  | 4.37                | 97.0              | 3.04                | 98.1              | 4.17                | 97.0              | 10.6                | 88.2              | 34.0                | 39.3           | 33.5 | 45.6 | -    |
| AerialMD. only                             | 6.33                | 95.6              | 4.39                | 97.1              | -                   | -                  | 4.55                | 96.0              | 3.25                | 97.7              | 4.48                | 96.4              | 11.5                | 87.8              | 41.0                | 58.7           | 38.3 | 65.3 | -    |
| MegaSc. only                               | 6.68                | 94.5              | 4.61                | 96.8              | -                   | -                  | 5.13                | 94.9              | 3.59                | 97.2              | 4.82                | 96.0              | 9.99                | 89.8              | 32.4                | 53.0           | 28.7 | 61.9 | -    |
| AerialMD.+MegaSc.                          | 6.66                | 95.2              | 4.52                | 97.0              | -                   | -                  | 4.86                | 95.5              | 3.43                | 97.5              | 4.66                | 96.2              | 9.57                | 91.0              | 32.7                | 65.0           | 26.4 | 74.7 | -    |

via relative depth error ( $Rel^d$ ) and depth inlier percentage ( $\delta_1^d$ ). Additionally, for methods that accept external camera parameters, we evaluate metric depth estimation using ground-truth camera intrinsics to isolate depth accuracy from errors in intrinsic parameter estimation. Results are in Tab. 1 (right side). While slightly worse than MoGe-2 on these metrics, WildMoGe outperforms most of the other baselines. This slight performance drop can be ascribed to the domain shift, and could be remedied by joint training. On the MetricScenes test set, WildMoGe outperforms MoGe-2 across all metrics. This suggests that while there is a trade-off on legacy datasets due to domain shift, the model successfully overcomes the scale-collapse phenomenon to achieve superior accuracy in unconstrained, in-the-wild environments.

**Fine-tuning on Different Subsets.** The ablation results in Tab. 2 validate the multi-source design of the MetricScenes dataset by showing how each subset contributes to performance. Each ablated model is trained for 3 epochs, consistent with the WildMoGe training schedule. On the standard benchmarks, we observe that each data source addresses a specific aspect of the model’s performance. Specifically, Stereo4D helps improve boundary sharpness ( $F_1 = 15.6$ ); AerialMegaDepth serves as a reliable metric anchor, resulting in strong metric-scale geometry accuracy; MegaScenes adds important perspective diversity, and when combined with AerialMegaDepth, achieves the lowest scale-invariant point error, which helps the model handle many different camera viewpoints. Generally, we find that joint training on the full corpus leads to better metric geometry and sharper boundaries. On the MetricScenes test set, we find that training exclusively on each subset tends to limit overall performance. In contrast, joint training across all subsets achieves superior results across every metric, suggesting a strong synergistic effect.

## 5 Conclusion

In this work, we identify scale collapse as a challenge in monocular metric depth/geometry estimation on in-the-wild scenes. Despite the impressive per-

formance of modern models on standard benchmarks, they often fail to maintain consistent real-world dimensions on certain types of data, such as distant landmarks or vast landscapes. We consider this fundamentally a data problem rooted in the limited scale diversity of existing training sets, which are typically restricted by hardware constraints or a lack of semantic complexity. To bridge this gap, we propose MetricScenes, a diverse and metrically-grounded real-world dataset curated from widely available sources including Internet photo collections and online stereo videos/imagery. Through qualitative and quantitative evaluations, we found that fine-tuning the state-of-the-art MoGe-2 model on our dataset effectively overcomes scale-collapse, enabling faithful metric scale recovery in unconstrained environments while maintaining competitive performance on standard benchmarks.

## References

1. Baruch, G., Chen, Z., Dehghan, A., Dimry, T., Feigin, Y., Fu, P., Gebauer, T., Joffe, B., Kurz, D., Schwartz, A., Shulman, E.: ARKitScenes: A diverse real-world dataset for 3d indoor scene understanding using mobile rgb-d data. ArXiv **abs/2111.08897** (2021)
2. Bhat, S.F., Birkel, R., Wofk, D., Wonka, P., Müller, M.: Zoedepth: Zero-shot transfer by combining relative and metric depth. arXiv preprint arXiv:2302.12288 (2023)
3. Bochkovskii, A., Delaunoy, A., Germain, H., Santos, M., Zhou, Y., Richter, S.R., Koltun, V.: Depth pro: Sharp monocular metric depth in less than a second. arXiv (2024), <https://arxiv.org/abs/2410.02073>
4. Butler, D.J., Wulff, J., Stanley, G.B., Black, M.J.: A naturalistic open source movie for optical flow evaluation. In: A. Fitzgibbon et al. (Eds.) (ed.) European Conf. on Computer Vision (ECCV). pp. 611–625. Part IV, LNCS 7577, Springer-Verlag (Oct 2012)
5. Cai, R., Tung, J., Wang, Q., Averbuch-Elor, H., Hariharan, B., Snavely, N.: Doppelgangers: Learning to disambiguate images of similar structures. In: Proceedings of the IEEE/CVF International Conference on Computer Vision. pp. 34–44 (2023)
6. Downs, L., Francis, A., Koenig, N., Kinman, B., Hickman, R., Reymann, K., McHugh, T.B., Vanhoucke, V.: Google scanned objects: A high-quality dataset of 3d scanned household items (2022)
7. Duisterhof, B.P., Žust, L., Weinzaepfel, P., Leroy, V., Cabon, Y., Revaud, J.: Mast3r-sfm: A fully-integrated solution for unconstrained structure-from-motion. 2025 International Conference on 3D Vision (3DV) pp. 1–10 (2024), <https://api.semanticscholar.org/CorpusID:272988049>
8. Fonder, M., Droogenbroeck, M.V.: Mid-air: A multi-modal dataset for extremely low altitude drone flights. 2019 IEEE/CVF Conference on Computer Vision and Pattern Recognition Workshops (CVPRW) pp. 553–562 (2019), <https://api.semanticscholar.org/CorpusID:156052231>
9. Guizilini, V., Ambrus, R., Pillai, S., Raventos, A., Gaidon, A.: 3d packing for self-supervised monocular depth estimation. In: IEEE Conference on Computer Vision and Pattern Recognition (CVPR) (2020)
10. Hu, M., Yin, W., Zhang, C., Cai, Z., Long, X., Chen, H., Wang, K., Yu, G., Shen, C., Shen, S.: Metric3d v2: A versatile monocular geometric foundation model for zero-shot metric depth and surface normal estimation. IEEE Transactions on Pattern Analysis and Machine Intelligence **46**(12), 10579–10596 (2024)

11. Jin, L., Tucker, R., Li, Z., Fouhey, D., Snavely, N., Holynski, A.: Stereo4D: Learning How Things Move in 3D from Internet Stereo Videos. In: CVPR (2025)
12. Jung, H., Ruhkamp, P., Zhai, G., Brasch, N., Li, Y., Verdie, Y., Song, J., Zhou, Y., Armagan, A., Ilic, S., et al.: On the importance of accurate geometry data for dense 3d vision tasks. In: Proceedings of the IEEE/CVF Conference on Computer Vision and Pattern Recognition. pp. 780–791 (2023)
13. Keetha, N., Müller, N., Schönberger, J., Porzi, L., Zhang, Y., Fischer, T., Knapitsch, A., Zauss, D., Weber, E., Antunes, N., Luiten, J., Lopez-Antequera, M., Bulò, S.R., Richardt, C., Ramanan, D., Scherer, S., Kotschieder, P.: MapAnything: Universal feed-forward metric 3D reconstruction. In: International Conference on 3D Vision (3DV). IEEE (2026)
14. Koch, T., Liebel, L., Fraundorfer, F., Körner, M.: Evaluation of cnn-based single-image depth estimation methods. In: Leal-Taixé, L., Roth, S. (eds.) Proceedings of the European Conference on Computer Vision Workshops (ECCV-WS). pp. 331–348. Springer International Publishing (2019)
15. Koch, T., Liebel, L., Körner, M., Fraundorfer, F.: Comparison of monocular depth estimation methods using geometrically relevant metrics on the ibims-1 dataset. *Computer Vision and Image Understanding (CVIU)* **191**, 102877 (2020). <https://doi.org/10.1016/j.cviu.2019.102877>
16. Leroy, V., Cabon, Y., Revaud, J.: Grounding image matching in 3d with mast3r. In: European Conference on Computer Vision. pp. 71–91. Springer (2024)
17. Li, Y., Jiang, L., Xu, L., Xiangli, Y., Wang, Z., Lin, D., Dai, B.: Matrixcity: A large-scale city dataset for city-scale neural rendering and beyond. 2023 IEEE/CVF International Conference on Computer Vision (ICCV) pp. 3182–3192 (2023), <https://api.semanticscholar.org/CorpusID:263135139>
18. Li, Y., Xiangli, Y., Averbuch-Elor, H., Snavely, N., Cai, R.: Long-tail internet photo reconstruction. In: Proceedings of the IEEE/CVF Conference on Computer Vision and Pattern Recognition (2026)
19. Li, Z., Snavely, N.: Megadepth: Learning single-view depth prediction from internet photos. In: Computer Vision and Pattern Recognition (CVPR) (2018)
20. Lin, H., Chen, S., Liew, J.H., Chen, D.Y., Li, Z., Shi, G., Feng, J., Kang, B.: Depth anything 3: Recovering the visual space from any views. ArXiv [abs/2511.10647](https://arxiv.org/abs/2511.10647) (2025), <https://api.semanticscholar.org/CorpusID:282992334>
21. Mehl, L., Schmalfluss, J., Jahedi, A., Nalivayko, Y., Bruhn, A.: Spring: A high-resolution high-detail dataset and benchmark for scene flow, optical flow and stereo. In: Proc. IEEE/CVF Conference on Computer Vision and Pattern Recognition (CVPR) (2023)
22. Nathan Silberman, Derek Hoiem, P.K., Fergus, R.: Indoor segmentation and support inference from rgb-d images. In: ECCV (2012)
23. Piccinelli, L., Sakaridis, C., Yang, Y.H., Segu, M., Li, S., Abbeloos, W., Gool, L.V.: Unidepth2: Universal monocular metric depth estimation made simpler (2025), <https://arxiv.org/abs/2502.20110>
24. Roberts, M., Paczan, N.: Hypersim: A photorealistic synthetic dataset for holistic indoor scene understanding. 2021 IEEE/CVF International Conference on Computer Vision (ICCV) pp. 10892–10902 (2020), <https://api.semanticscholar.org/CorpusID:226254406>
25. Schönberger, J.L., Frahm, J.M.: Structure-from-motion revisited. In: Conference on Computer Vision and Pattern Recognition (CVPR) (2016)
26. Schönberger, J.L., Zheng, E., Pollefeys, M., Frahm, J.M.: Pixelwise view selection for unstructured multi-view stereo. In: European Conference on Computer Vision (ECCV) (2016)

27. Schöps, T., Sattler, T., Pollefeys, M.: BAD SLAM: Bundle adjusted direct RGB-D SLAM. In: Conference on Computer Vision and Pattern Recognition (CVPR) (2019)
28. Sun, P., Kretzschmar, H., Dotiwalla, X., Chouard, A., Patnaik, V., Tsui, P., Guo, J., Zhou, Y., Chai, Y., Caine, B., Vasudevan, V., Han, W., Ngiam, J., Zhao, H., Timofeev, A., Ettinger, S.M., Krivokon, M., Gao, A., Joshi, A., Zhang, Y., Shlens, J., Chen, Z., Anguelov, D.: Scalability in perception for autonomous driving: Waymo open dataset. 2020 IEEE/CVF Conference on Computer Vision and Pattern Recognition (CVPR) pp. 2443–2451 (2019), <https://api.semanticscholar.org/CorpusID:209140225>
29. Tung, J., Chou, G., Cai, R., Yang, G., Zhang, K., Wetzstein, G., Hariharan, B., Snavely, N.: Megascenes: Scene-level view synthesis at scale. ArXiv **abs/2406.11819** (2024)
30. Uhrig, J., Schneider, N., Schneider, L., Franke, U., Brox, T., Geiger, A.: Sparsity invariant cnns. In: International Conference on 3D Vision (3DV) (2017)
31. Vasiljevic, I., Kolkin, N., Zhang, S., Luo, R., Wang, H., Dai, F.Z., Daniele, A.F., Mostajabi, M., Basart, S., Walter, M.R., Shakhnarovich, G.: DIODE: A Dense Indoor and Outdoor DEpth Dataset. CoRR **abs/1908.00463** (2019), <http://arxiv.org/abs/1908.00463>
32. Vuong, K., Ghosh, A., Ramanan, D., Narasimhan, S., Tulsiani, S.: Aerialmegadepth: Learning aerial-ground reconstruction and view synthesis. In: Proceedings of the IEEE/CVF Conference on Computer Vision and Pattern Recognition (2025)
33. Wang, R., Xu, S., Dong, Y., Deng, Y., Xiang, J., Lv, Z., Sun, G., Tong, X., Yang, J.: Moge-2: Accurate monocular geometry with metric scale and sharp details. arXiv preprint arXiv:2507.02546 (2025), <https://arxiv.org/abs/2507.02546>
34. Wang, W., Zhu, D., Wang, X., Hu, Y., Qiu, Y., Wang, C., Hu, Y., Kapoor, A., Scherer, S.A.: Tartanair: A dataset to push the limits of visual slam. 2020 IEEE/RSJ International Conference on Intelligent Robots and Systems (IROS) pp. 4909–4916 (2020), <https://api.semanticscholar.org/CorpusID:214727835>
35. Wang, Y., Zhou, J., Zhu, H., Chang, W., Zhou, Y., Li, Z., Chen, J., Pang, J., Shen, C., He, T.: Pi3: Permutation-equivariant visual geometry learning. arXiv preprint arXiv:2507.13347 (2025)
36. Wang, Y., Lipson, L., Deng, J.: Sea-raft: Simple, efficient, accurate raft for optical flow. In: European Conference on Computer Vision. pp. 36–54. Springer (2024)
37. Wen, B., Trepte, M., Aribido, J., Kautz, J., Gallo, O., Birchfield, S.: Foundation-stereo: Zero-shot stereo matching. In: Proceedings of the IEEE/CVF conference on computer vision and pattern recognition. pp. 5249–5260 (2025)
38. Wilson, B., Qi, W., Agarwal, T., Lambert, J., Singh, J., Khandelwal, S., Pan, B., Kumar, R., Hartnett, A., Pontes, J.K., Ramanan, D., Hays, J.: Argoverse 2: Next generation datasets for self-driving perception and forecasting. ArXiv **abs/2301.00493** (2023)
39. Wrenninge, M., Unger, J.: Synscapes: A photorealistic synthetic dataset for street scene parsing. ArXiv **abs/1810.08705** (2018), <https://api.semanticscholar.org/CorpusID:53047282>
40. Xiangli, Y., Cai, R., Chen, H., Byrne, J., Snavely, N.: Doppelgangers++: Improved visual disambiguation with geometric 3d features (2025)
41. Yang, L., Kang, B., Huang, Z., Zhao, Z., Xu, X., Feng, J., Zhao, H.: Depth anything v2. In: NeurIPS (2024)

42. Yao, Y., Luo, Z., Li, S., Zhang, J., Ren, Y., Zhou, L., Fang, T., Quan, L.: Blend-edmvs: A large-scale dataset for generalized multi-view stereo networks. 2020 IEEE/CVF Conference on Computer Vision and Pattern Recognition (CVPR) pp. 1787–1796 (2019), <https://api.semanticscholar.org/CorpusID:208248003>
43. Yeshwanth, C., Liu, Y.C., Nießner, M., Dai, A.: Scannet++: A high-fidelity dataset of 3d indoor scenes. 2023 IEEE/CVF International Conference on Computer Vision (ICCV) pp. 12–22 (2023), <https://api.semanticscholar.org/CorpusID:261064784>
44. Yin, W., Zhang, C., Chen, H., Cai, Z., Yu, G., Wang, K., Chen, X., Shen, C.: Metric3d: Towards zero-shot metric 3d prediction from a single image. 2023 IEEE/CVF International Conference on Computer Vision (ICCV) pp. 9009–9019 (2023), <https://api.semanticscholar.org/CorpusID:259991083>
45. Yin, W., Zhang, J., Wang, O., Niklaus, S., Mai, L., Chen, S., Shen, C.: Learning to recover 3d scene shape from a single image. 2021 IEEE/CVF Conference on Computer Vision and Pattern Recognition (CVPR) pp. 204–213 (2020), <https://api.semanticscholar.org/CorpusID:229298063>

# Supplemental Material for Honey, I Shrunk the Arc de Triomphe!

## 1 Curate Geo-tagged Images

In Fig. 1 we visualize the distribution of collected geo-tagged images for MegaScenes 17. Specifically, these images are curated through the following pipeline:

We first retrieve the scene’s bounding polygon and key navigation points via mapping system APIs. Because raw polygon vertices are typically sparse, we interpolate these outlines to create a dense series of reference points. These points act as spatial anchors for localized queries to identify the surrounding environment, including road networks, walkable paths, and neighboring building footprints, transforming an isolated footprint into a grounded, context-aware map.

Using this environmental map, we aggregate candidate coordinates from diverse sources to ensure comprehensive coverage of all facades. These candidates include positions offset from the scene boundary, points sampled along adjacent roads and paths, and stochastically generated coordinates within the immediate vicinity.

To mitigate occlusions, we implement a visibility filter. For each candidate, we cast a ray toward the nearest point on the target scene’s outline; if the ray intersects any intervening obstacle polygons (neighboring structures), the viewpoint is discarded. For validated coordinates, the camera heading is computed as the vector from the viewpoint to the nearest point on the scene boundary.

Finally, we exclusively select standardized, professionally captured geo-tagged images that match these calculated headings, excluding inconsistent crowd-sourced data to ensure high-fidelity inputs for 3D reconstruction. From this pool of geo-tagged images, we sample 100 roughly evenly distributed views for geo-registration.

## 2 SfM Disambiguation and Depth Refinement

### 2.1 Filtering and Disambiguation

We notice that compared to AerialMegaDepth 19, scenes in MegaScenes 17 are more likely to suffer from doppelganger issues 2. The ground-level nature of these images often lacks the global context required to disambiguate repetitive structures, leading to erroneous matches. To mitigate this, we employ MAST3R-SfM 9 in conjunction with a Doppelganger classifier 25 instead of the conventional COLMAP pipeline. In our implementation, the classifier prunes ambiguous edges in the MAST3R-derived scene graph to eliminate false correspondences. We further filter the dataset through geo-spatial verification, discarding

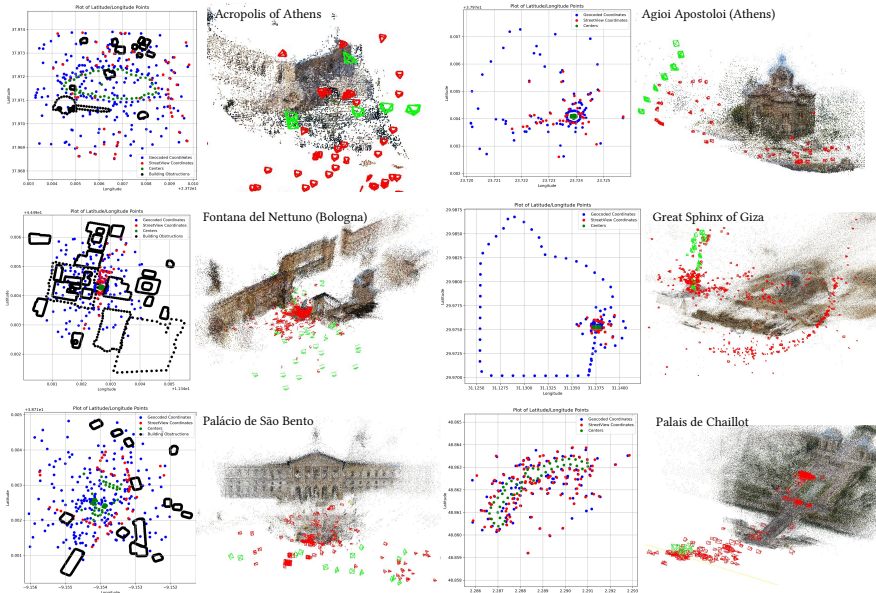


**Fig. 1: Geo-tagged images distribution visualization.** Column 1&3 are plots of building outlines and nearby geo-tagged images. From building outlines, we generate a dense series of viewpoint coordinates (green boxes dots) as virtual camera locations to ensure full-facade coverage. From these virtual camera locations, we expand the search to surrounding environments where images are likely to be taken (blue dots), such as road networks and walkable paths. To account for urban density, we identify neighboring building footprints as potential obstructions (black dots). By applying a visibility filter that discards any viewpoint with an interrupted line-of-sight, we arrive at our final set of validated, geo-tagged image positions (red dots), which provide an unobstructed view of the target landmark. Column 2&4 show corresponding reconstruction components with geo-tagged views marked green frustums, and MegaScenes views marked red frustums.

reconstructions whose registered camera positions are inconsistent with their metadata-based geographic distributions.

## 2.2 Dense Depth Refinement

Following sparse reconstruction, we generate dense depth maps for supervision using a standard Multi-View Stereo (MVS) [15] pipeline. As observed in prior studies [10], raw geometric depth maps derived from unconstrained, “in-the-wild” collections often exhibit severe artifacts. These include *depth-bleeding*—where background depths erroneously leak into foreground regions—and significant noise in areas occupied by transient objects (*e.g.*, pedestrians or vehicles).

To address these issues, we initially adopt the refinement strategy from MegaDepth, which incorporates conservative depth propagation, stability filtering, and semantic masking. However, several challenges persist: the modified MVS remains insufficient for suppressing bleeding artifacts at complex occlusion

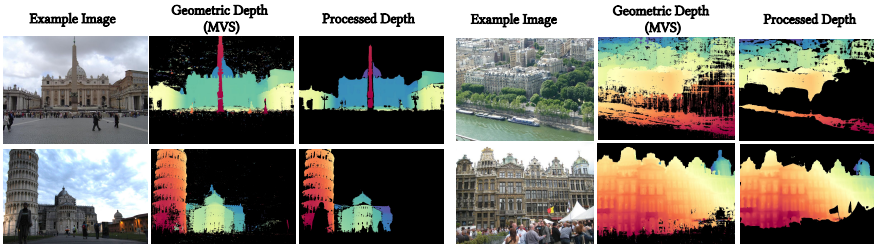


**Fig. 2: Dense Depth Refinement.** Geometric depth maps from MVS (second and fifth columns) often suffer from geometric noise in unconstrained outdoor scenes. By incorporating monocular-guided filtering and stability checks, our processed depth (third and sixth columns) obtains cleaner boundary and effectively masks out transient regions, ensuring that only high-confidence depth regions are retained.

boundaries, and semantic filtering is limited by its reliance on a manually curated list of object categories. Therefore, we further leverage depth predictions from MoGe-2 [20] as ordinal depth priors to identify and exclude inconsistent pixels in the geometric depth maps. Specifically, we first align the geometric depths  $D_{\text{geom}}$  to the monocular predictions  $D_{\text{mono}}$  by matching their median values over valid pixels  $P$ :

$$D'_{\text{geom}}(p) = s \cdot D_{\text{geom}}(p), \quad \text{where } s = \frac{\text{med}\{D_{\text{mono}}(p) \mid p \in P\}}{\text{med}\{D_{\text{geom}}(p) \mid p \in P\}}. \quad (1)$$

After scale alignment, we quantify the normalized discrepancy between the two maps:

$$\Delta(p) = \frac{|D'_{\text{geom}}(p) - D_{\text{mono}}(p)|}{D'_{\text{geom}}(p)}. \quad (2)$$

Pixels exceeding a predefined threshold  $\tau$  are discarded to ensure high-fidelity supervision:

$$D_{\text{refined}}(p) = \begin{cases} D_{\text{geom}}(p) & \text{if } p \in P \text{ and } \Delta(p) \leq \tau, \\ \text{NaN} & \text{otherwise.} \end{cases} \quad (3)$$

This cross-modal filtering strategy effectively suppresses both bleeding artifacts and transient object noise without requiring explicit category-specific heuristics. Examples are shown in Fig. 2.

## 3 Implementation Details

### 3.1 FG/BG Separation Strategy

Depth maps from COLMAP MVS typically only contain the landmark of interest without transient foreground objects, so we mark all valid MVS depth pixels as BG. For the FG, we introduce a dynamic depth threshold based on the severity of the scale mismatch. We compute a robust scale factor  $s$  that aligns the MVS

depth to the MoGe-2 depth, and then compute a fraction  $p = 0.8 \cdot \min(s, 1/s)$ . All pixels with a MoGe-2 depth less than  $ps \cdot \min\{d^{BG}\}$  are FG, where  $\min\{d^{BG}\}$  is the minimum BG depth in the MVS depth map. Intuitively, the transition region between FG and BG should be large when the scale mismatch is high, giving Poisson completion ample space to reconcile the mismatch, and small when it is low, so that structural details from the MoGe-2 depth are maximally preserved.

### 3.2 Training Configurations

We fine-tune the MoGe-2 [21] ViT-Large-Normal model on our MetricScenes dataset for 10,000 iterations with a batch size of 32 (approximately 3 epochs), ensuring model convergence while preventing significant divergence from the pre-trained geometric priors. We use a learning rate of  $1 \times 10^{-6}$  for the backbone and  $1 \times 10^{-5}$  for the remaining parameters. The model is optimized with Adam optimizer [5]. We adopt MoGe [20] and MoGe-2’s approach for image cropping and data augmentation.

To set the sampling weights among different training subsets, we adopt an empirical dataset weighting strategy with a sampling ratio of 2:2:1 for AerialMegaDepth, MegaScenes, and Stereo4D, respectively. We adopt this weighting because, unlike MoGe and MoGe-2 which employ 2D feature-matching against general image distributions (*e.g.*, OpenImages [8]) to balance dozens of heterogeneous datasets, our training corpus consists of three carefully curated subsets specifically targeted at resolving scale-collapse. Furthermore, purely visual retrieval metrics do not account for the quality or reliability of the underlying 3D geometry. Therefore, we do not strictly follow their strategy of deriving sampling probabilities from visual nearest-neighbor searches against uncalibrated photos. Instead, our empirical ratio ensures the model prioritizes the high-quality, metrically anchored data necessary to learn absolute scale in expansive scenes, rather than diluting the training signal by forcing alignment to a generic 2D image distribution.

## 4 Evaluation Protocol

We follow the evaluation protocol of alignment in MoGe [20] and MoGe-2 [21]. For all our models and baselines, predictions and ground truth are aligned in scale (and shift, if applicable) for each image before measuring errors. Specifically, for relative geometry evaluation:

- $\hat{\mathbf{p}}_i$  and  $\mathbf{p}_i$  are the predicted and ground-truth points, respectively.
- $\hat{z}_i$  and  $z_i$  are the predicted and ground-truth depths, which are the  $Z$ -coordinate of corresponding points.
- $\mathcal{M}$  is the mask of valid ground-truth.
- $a$  and  $b$  denote the scale and shift used to align predictions with the ground truth for evaluation, to avoid confusion with similar symbols used in the training objectives.

- **Scale-invariant point map.** The scale  $a^*$  to align prediction with ground truth is computed as:

$$a^* = \operatorname{argmin}_a \sum_{i \in \mathcal{M}} \frac{1}{z_i} \|a\hat{\mathbf{p}}_i - \mathbf{p}_i\|_1, \quad (4)$$

- **Affine-invariant point map.** The scale  $a^*$  and shift  $\mathbf{b}^*$  are computed as:

$$(a^*, \mathbf{b}^*) = \operatorname{argmin}_{a, \mathbf{b}} \sum_{i \in \mathcal{M}} \frac{1}{z_i} \|a\hat{\mathbf{p}}_i + \mathbf{b} - \mathbf{p}_i\|_1. \quad (5)$$

- **Scale-invariant depth map,** the scale  $a^*$  is computed as

$$a^* = \operatorname{argmin}_s \sum_{i \in \mathcal{M}} \frac{1}{z_i} |a\hat{z}_i - z_i|. \quad (6)$$

- **Affine-invariant depth map.** The scale  $a^*$  and shift  $b^*$  are computed as

$$(a^*, b^*) = \operatorname{argmin}_s \sum_{i \in \mathcal{M}} \frac{1}{z_i} |a\hat{z}_i + b - z_i|. \quad (7)$$

- **Affine-invariant disparity map.** We follow the established protocol for affine disparity alignment [14], using least-squares to align predictions in disparity space:

$$(a^*, b^*) = \operatorname{argmin}_s \sum_{i \in \mathcal{M}} (a\hat{d}_i + b - d_i)^2, \quad (8)$$

where  $\hat{d}_i$  is the predicted disparity and  $d_i$  is the ground truth, defined as  $d_i = 1/z_i$ . To prevent aligned disparities from taking excessively small or negative values, the aligned disparity is truncated by the inverted maximum depth  $1/z_{\max}$  before inversion. The final aligned depth  $\hat{z}_i^*$  is computed as:

$$\hat{z}_i^* := \frac{1}{\max(a^*\hat{d}_i + b^*, 1/z_{\max})}. \quad (9)$$

For metric geometry:

- **Metric depth.** The output is evaluated without alignment and clamping range of values for all methods, unless specific post-processing is hard-coded in its model inference pipeline.
- **Metric point map.** The point map prediction is aligned with the ground truth by the optimal translation:

$$\mathbf{b}^* = \operatorname{argmin}_{\mathbf{b}} \sum_{i \in \mathcal{M}} \frac{1}{z_i} \|\hat{\mathbf{p}}_i + \mathbf{b} - \mathbf{p}_i\|_1. \quad (10)$$

## 5 More Ablations

### 5.1 Train on Partial Depth Maps

Fine-tuning with partial depth maps leads to incomplete results or erroneous foreground depth, as illustrated in Fig. 3. We show relative depth maps for visual clarity. While MoGe-2 learns mask, scale, and local/global depth, we evaluate two supervision strategies: (1) Middle: mask, scale, and local/global depth are supervised using partial depth maps. (2) Right: Scale and global depth are supervised with partial depth maps, while mask and local depth are supervised with MoGe-2’s predictions so that the mask isn’t learned from incomplete depth data.

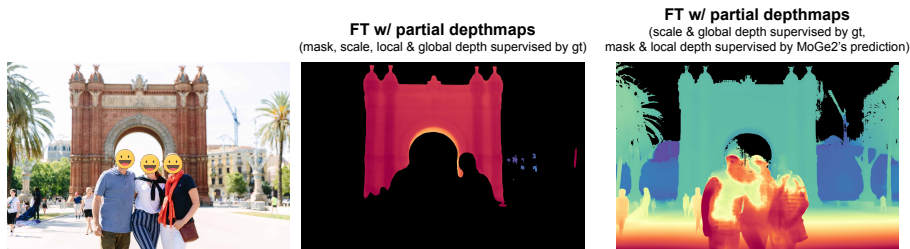


**Fig. 3:** Fine-tuning MoGe-2 on partial depth (i.e., depth maps prior to two-stage completion) yields incomplete structures or erroneous foreground depth.

### 5.2 Comparison of Depth Completion Methods

Fig. 4 shows visual comparisons of our two-stage Poisson completion pipeline against state-of-the-art depth completion methods across diverse outdoor environments. To ensure a fair comparison, input anchors to Marigold-DC [18] and Prompt-DA [12] are a combination of MoGe-2 foreground depths and filtered MVS background depths, which provide both foreground and background scale guidance. For Prompt-DA, we follow their preprocessing strategy and further fill in missing depth values in the input with KNN completion. Since the depth completion methods do not output any confidence measure, we use SegFormer [26] to filter out sky pixels in the output depth maps.

We observe that diffusion-based approaches like Marigold-DC [18] introduce significant surface noise and struggle to recover clean, accurate depth for cluttered foreground objects. Prompt-DA [12] exhibits even more pronounced scale drift and oversmoothing, particularly in unconstrained regions (e.g., crowds in the foreground and edges of buildings), leading to massive geometric distortions. As a feedforward method, it also fails to accurately preserve ground truth anchors in the output depth map. In contrast, our method consistently produces dense depth maps with high structural fidelity. It not only preserves sharp occlusion boundaries but also maintains global metric consistency, effectively bridging the gap between sparse reconstruction and dense, scale-aware depth estimation.

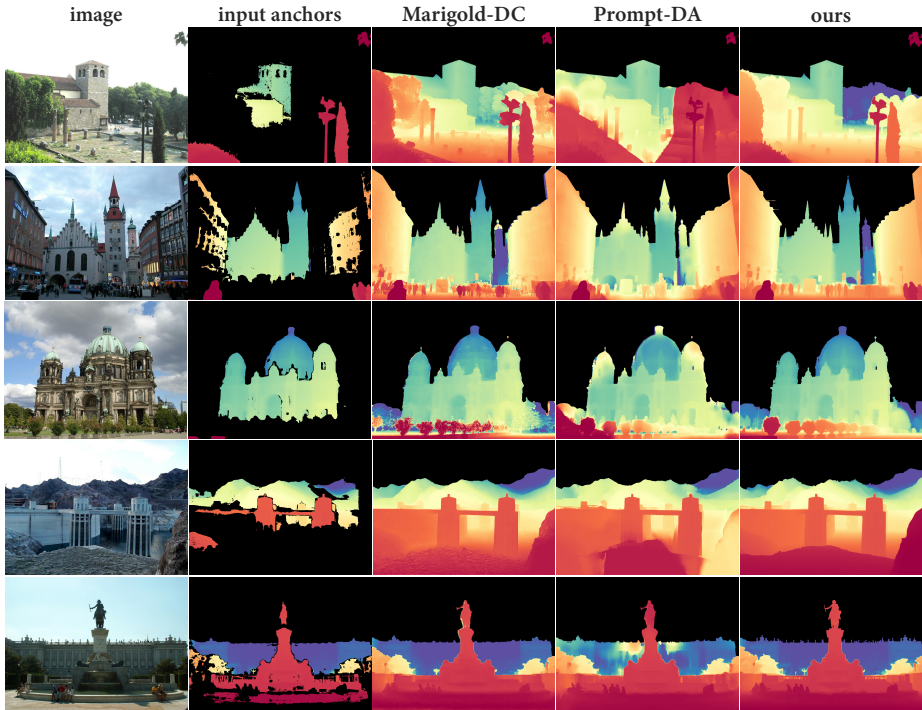


**Fig. 4: Visual comparison of depth completion methods.** We compare our two-stage Poisson completion pipeline against recent depth completion methods. The input anchors are a combination of MoGe-2 foregrounds and filtered MVS backgrounds. Both Marigold-DC [18] and Prompt-DA [12] struggle to recover accurate metric depth in unanchored regions. As a diffusion-based model, Marigold-DC produces high amounts of surface noise. Meanwhile, Prompt-DA suffers from even more severe scale drift, yielding massive geometric errors in the resulting depth maps even in regions constrained by input anchors. Our approach reliably produces accurate metric depth throughout the scene while preserving sharp boundaries.

### 5.3 Comparison of Stereo & Multi-View Methods

Fig. 5 provides more visual comparisons of reconstruction quality across various state-of-the-art stereo matching and multi-view reconstruction methods. As illustrated in the magenta boxes, dedicated two-view stereo matching methods (e.g., SEA-RAFT [23], FoundationStereo [24]) are highly susceptible to imperfectly calibrated in-the-wild video sequences. These extrinsic calibration errors manifest as severe surface distortions, such as warped roofs and fractured wall structures, and the entire scene being shrunk down. While multi-view methods like DA 3 [11] and MapAnything [4] improve global consistency, they frequently exhibit artifacts around complex foreground subjects. As shown in the black circle inlays, these methods often smear or distort pedestrians, failing to maintain sharp object boundaries. In contrast,  $\pi^3$  produces the most robust and geomet-

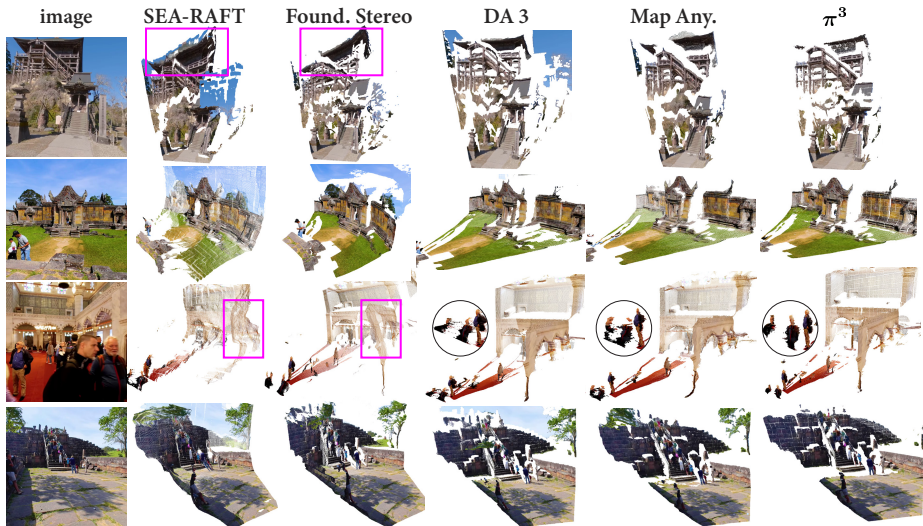


**Fig. 5: Visual comparison of stereo matching & multi-view reconstruction methods.** Dedicated two-view stereo matching methods (SEA-RAFT [23], FoundationStereo [24]) struggle with imperfectly calibrated in-the-wild videos, resulting in severe surface distortions such as warped roofs and walls (magenta boxes). Multi-view reconstruction methods [4, 22, 27] generally improve global structural consistency. Among these methods,  $\pi^3$  [22] produces the most robust geometry, while other methods often smear or distort foreground subjects like people (black circle inlays).

rically faithful results, successfully recovering clean architectural structures and preserving the integrity of foreground subjects even under challenging unconstrained conditions.

#### 5.4 Evaluation on Individual Test Subsets

We evaluate WildMoGe and its variations (*i.e.* MoGe-2 fine-tuned on different subsets of MetricScenes) on each individual test sets of MetricScenes. Results are presented in Tab. 1. This study demonstrates that while domain-specific models achieve peak performance on their native benchmarks, the “All” model provides the most robust balance between relative and metric geometry across diverse scenes. In terms of relative geometry, the “All” model consistently ranks as best or second-best across all test sets, proving that diverse training data facilitates a more generalized understanding of scene shape. Its superiority is most evident in metric geometry, where it effectively prevents the scale-collapse phenomenon. This failure is exemplified by the “Stereo4D only” model, which exhibits an extreme metric error when evaluated on the AerialMegaDepth set. In contrast, the “All” model maintains stable metric recovery across all environments. These results justify the necessity of the full MetricScenes dataset for achieving reliable, real-world metric recovery in unconstrained environments.

**Table 1: Ablation of finetuning MoGe-2 using different subsets of MetricScenes.** Evaluation is conducted on each individual subsets of MetricScenes’s test set. We evaluate performance across relative geometry and metric geometry. Metrics are color-coded: **red** (best) and **yellow** (second best).

| Method                                       | Relative Geometry           |                                   |                                   |                             |                                   |                                   |                                     |  |                               | Metric Geometry                    |                               |                                    |                              |                                   |      |      |
|--|-----------------------------|-----------------------------------|-----------------------------------|-----------------------------|-----------------------------------|-----------------------------------|-------------------------------------|--|-------------------------------|------------------------------------|-------------------------------|------------------------------------|------------------------------|-----------------------------------|------|------|
|  | Point                       |                                   |                                   | Depth                       |                                   |                                   | Point                               |  |                               | Depth                              |                               |                                    |                              |                                   |      |      |
|  | Scale-inv. Rel $\downarrow$ | Affine-inv. $\delta_1^p \uparrow$ | Affine-inv. $\delta_1^p \uparrow$ | Scale-inv. Rel $\downarrow$ | Affine-inv. $\delta_1^d \uparrow$ | Affine-inv. $\delta_1^d \uparrow$ | Affine-inv. (disp) Rel $\downarrow$ | Affine-inv. (disp) $\delta_1^d \uparrow$ | (w/o GT Cam) Rel $\downarrow$ | (w/o GT Cam) $\delta_1^p \uparrow$ | (w/o GT Cam) Rel $\downarrow$ | (w/o GT Cam) $\delta_1^d \uparrow$ | (w/ GT Cam) Rel $\downarrow$ | (w/ GT Cam) $\delta_1^d \uparrow$ |      |      |
| <i>Evaluated on AerialMegaDepth Test Set</i> |                             |                                   |                                   |                             |                                   |                                   |                                     |  |                               |                                    |                               |                                    |                              |                                   |      |      |
| All  | 3.28                        | 99.0                              | 2.27                              | 99.3                        | 2.61                              | 99.0                              | 1.93                                | 99.4                                     | 2.70                          | 98.7                               | 3.65                          | 98.8                               | 10.4                         | 89.4                              | 8.76 | 94.1 |
| Stereo4D only                                | 4.85                        | 98.6                              | 2.69                              | 99.1                        | 3.39                              | 98.7                              | 2.19                                | 99.2                                     | 2.96                          | 98.6                               | 15.5                          | 78.9                               | 52.5                         | 5.53                              | 47.0 | 10.8 |
| AerialMD. only                               | 2.88                        | 99.2                              | 2.10                              | 99.4                        | 2.33                              | 99.2                              | 1.79                                | 99.5                                     | 2.51                          | 98.8                               | 3.13                          | 99.1                               | 8.56                         | 94.3                              | 6.99 | 97.5 |
| MegaSc. only                                 | 3.68                        | 98.6                              | 2.68                              | 99.0                        | 2.68                              | 99.0                              | 2.92                                | 98.5                                     | 3.14                          | 98.3                               | 8.27                          | 93.5                               | 27.9                         | 33.2                              | 25.4 | 38.2 |
| AerialMD.+MegaSc.                            | 3.14                        | 99.1                              | 2.27                              | 99.3                        | 2.55                              | 99.1                              | 1.93                                | 99.4                                     | 2.77                          | 98.5                               | 3.90                          | 98.6                               | 11.4                         | 86.3                              | 9.84 | 90.2 |
| <i>Evaluated on MegaScenes Test Set</i>      |                             |                                   |                                   |                             |                                   |                                   |                                     |  |                               |                                    |                               |                                    |                              |                                   |      |      |
| All  | 4.50                        | 97.5                              | 2.14                              | 98.7                        | 2.79                              | 97.9                              | 1.50                                | 99.3                                     | 1.74                          | 99.5                               | 10.1                          | 90.4                               | 50.0                         | 59.0                              | 45.1 | 67.2 |
| Stereo4D only                                | 6.19                        | 96.8                              | 2.45                              | 98.6                        | 3.22                              | 97.8                              | 1.57                                | 99.4                                     | 1.76                          | 99.5                               | 7.63                          | 93.6                               | 41.8                         | 27.1                              | 40.2 | 39.1 |
| AerialMD. only                               | 3.98                        | 97.2                              | 2.12                              | 98.5                        | 2.58                              | 97.9                              | 1.47                                | 99.3                                     | 1.70                          | 99.5                               | 13.4                          | 85.2                               | 68.3                         | 50.5                              | 62.9 | 55.4 |
| MegaSc. only                                 | 4.19                        | 96.7                              | 2.05                              | 98.9                        | 2.81                              | 97.6                              | 1.49                                | 99.2                                     | 1.75                          | 99.3                               | 7.58                          | 92.7                               | 43.1                         | 65.8                              | 39.2 | 78.1 |
| AerialMD.+MegaSc.                            | 4.01                        | 97.3                              | 2.13                              | 98.8                        | 2.68                              | 98.1                              | 1.49                                | 99.3                                     | 1.75                          | 99.5                               | 8.15                          | 92.3                               | 49.5                         | 58.8                              | 42.8 | 69.7 |
| <i>Evaluated on Stereo4D Test Set</i>        |                             |                                   |                                   |                             |                                   |                                   |                                     |  |                               |                                    |                               |                                    |                              |                                   |      |      |
| All  | 7.94                        | 94.4                              | 6.59                              | 95.6                        | 6.67                              | 94.2                              | 5.51                                | 95.8                                     | 8.01                          | 92.9                               | 8.98                          | 92.1                               | 14.0                         | 82.9                              | 8.76 | 94.1 |
| Stereo4D only                                | 7.63                        | 94.6                              | 6.35                              | 95.3                        | 6.49                              | 94.5                              | 5.33                                | 95.7                                     | 7.78                          | 92.9                               | 8.64                          | 92.2                               | 13.3                         | 85.2                              | 11.7 | 86.9 |
| AerialMD. only                               | 12.1                        | 90.5                              | 8.95                              | 93.3                        | 8.71                              | 90.9                              | 6.48                                | 94.4                                     | 9.22                          | 90.9                               | 18.1                          | 79.1                               | 41.6                         | 38.3                              | 29.7 | 90.3 |
| MegaSc. only                                 | 12.2                        | 88.3                              | 9.11                              | 92.4                        | 9.66                              | 88.5                              | 7.09                                | 93.3                                     | 9.58                          | 90.5                               | 14.1                          | 83.3                               | 26.2                         | 60.0                              | 21.5 | 69.3 |
| AerialMD.+MegaSc.                            | 12.9                        | 89.8                              | 9.15                              | 92.9                        | 9.37                              | 89.4                              | 6.86                                | 93.9                                     | 9.48                          | 90.6                               | 16.7                          | 81.5                               | 37.2                         | 50.0                              | 26.7 | 64.3 |

## 5.5 Validate MetricScenes on Other Models

We also fine-tune DA V2 and Metric3D V2 on our dataset, with results reported in Tab. 2. Overall, fine-tuning on MetricScenes significantly improves these models’ performance on in-the-wild scenes and also yields gains on standard benchmarks in some cases. Note that on our test set, we evaluate DA V2 finetuned on KITTI (rather than the version finetuned on the indoor Hypersim dataset) because most scenes are outdoor. However, this KITTI-trained model still struggles because it has an effective depth range limited to 80m. In our fine-tuned version, we extend the effective depth range to 1km.

**Table 2: Fine-tuning DA V2 and Metric3D V2 on MetricScenes.** We show that fine-tuning on our dataset significantly improves these models’ performance on in-the-wild scenes and also yields gains on standard benchmarks in some cases.

| Method           | GT Cam? | Standard Benchmarks |                     | MetricScenes     |                     |
|------------------|---------|---------------------|---------------------|------------------|---------------------|
|                  |         | Rel $\downarrow$    | $\delta_1 \uparrow$ | Rel $\downarrow$ | $\delta_1 \uparrow$ |
| DA V2            | No      | 29.9                | 56.6                | 92.3             | 10.3                |
| DA V2 (FT)       | No      | 28.5                | 51.7                | 36.3             | 37.7                |
| Metric3D V2      | Yes     | 18.3                | 73.9                | 35.5             | 55.0                |
| Metric3D V2 (FT) | Yes     | 15.0                | 80.7                | 28.9             | 63.1                |

## 6 More Results

**Qualitative and Metrology Comparisons.** Fig. 6 presents additional qualitative and metrology results comparing MoGe-2 and WildMoGe where ground

truth is available. In in-the-wild scenes, MoGe-2 exhibits scale collapse, predicting a smaller scale for either the entire scene or its background. On standard benchmarks, such as ETH3D [16], both methods yield comparable results, though WildMoGe demonstrates higher accuracy and better alignment with the ground truth. For indoor scenes and objects, both models provide similar estimations.

**Boundary Sharpness Analysis.** Notably, after fine-tuning on MetricScenes, the model experiences a slight reduction in boundary sharpness. It achieves an average F1 score of 15.6 for boundary sharpness, compared to 16.3 for MoGe-2, when evaluated on iBims-1 [6, 7], Sintel [1], Spring [13], and HAMMER [3]. We hypothesize that joint training with additional synthetic data could mitigate this issue.

## 7 Discussion and Future Work

While this work demonstrates that fine-tuning MoGe-2 on MetricScenes can mitigate the scale-collapse phenomenon, our current approach relies on a direct fine-tuning schedule that introduces a slight performance trade-off on standard indoor benchmarks due to domain shift. Future research will explore more delicate training designs, such as sophisticated joint training regimes or adaptive data-mixing strategies, to maintain peak performance on the standard datasets while leveraging the diverse scale supervision of our new corpus. Furthermore, we envision MetricScenes serving as a foundational resource for training feed-forward, metric-scale multi-view reconstruction models like VGGT or  $\pi^3$ , enabling these models to recover absolute physical dimensions without the need for post-optimization.

## References

1. Butler, D.J., Wulff, J., Stanley, G.B., Black, M.J.: A naturalistic open source movie for optical flow evaluation. In: A. Fitzgibbon et al. (Eds.) (ed.) European Conf. on Computer Vision (ECCV). pp. 611–625. Part IV, LNCS 7577, Springer-Verlag (Oct 2012)
2. Cai, R., Tung, J., Wang, Q., Averbuch-Elor, H., Hariharan, B., Snavely, N.: Doppelgangers: Learning to disambiguate images of similar structures. In: Proceedings of the IEEE/CVF International Conference on Computer Vision. pp. 34–44 (2023)
3. Jung, H., Ruhkamp, P., Zhai, G., Brasch, N., Li, Y., Verdie, Y., Song, J., Zhou, Y., Armagan, A., Ilic, S., et al.: On the importance of accurate geometry data for dense 3d vision tasks. In: Proceedings of the IEEE/CVF Conference on Computer Vision and Pattern Recognition. pp. 780–791 (2023)
4. Keetha, N., Müller, N., Schönberger, J., Porzi, L., Zhang, Y., Fischer, T., Knapitsch, A., Zauss, D., Weber, E., Antunes, N., Luiten, J., Lopez-Antequera, M., Bulò, S.R., Richardt, C., Ramanan, D., Scherer, S., Kotschieder, P.: MapAnything: Universal feed-forward metric 3D reconstruction. In: International Conference on 3D Vision (3DV). IEEE (2026)

5. Kingma, D.P., Ba, J.: Adam: A method for stochastic optimization. CoRR **abs/1412.6980** (2014), <https://api.semanticscholar.org/CorpusID:6628106>
6. Koch, T., Liebel, L., Fraundorfer, F., Körner, M.: Evaluation of cnn-based single-image depth estimation methods. In: Leal-Taixé, L., Roth, S. (eds.) Proceedings of the European Conference on Computer Vision Workshops (ECCV-WS). pp. 331–348. Springer International Publishing (2019)
7. Koch, T., Liebel, L., Körner, M., Fraundorfer, F.: Comparison of monocular depth estimation methods using geometrically relevant metrics on the ibims-1 dataset. *Computer Vision and Image Understanding (CVIU)* **191**, 102877 (2020). <https://doi.org/10.1016/j.cviu.2019.102877>
8. Kuznetsova, A., Rom, H., Alldrin, N.G., Uijlings, J.R.R., Krasin, I., Pont-Tuset, J., Kamali, S., Popov, S., Mallocci, M., Kolesnikov, A., Duerig, T., Ferrari, V.: The open images dataset v4. *International Journal of Computer Vision* **128**, 1956 – 1981 (2018), <https://api.semanticscholar.org/CorpusID:53296866>
9. Leroy, V., Cabon, Y., Revaud, J.: Grounding image matching in 3d with mast3r (2024)
10. Li, Z., Snavely, N.: Megadepth: Learning single-view depth prediction from internet photos. In: *Computer Vision and Pattern Recognition (CVPR)* (2018)
11. Lin, H., Chen, S., Liew, J.H., Chen, D.Y., Li, Z., Shi, G., Feng, J., Kang, B.: Depth anything 3: Recovering the visual space from any views. ArXiv **abs/2511.10647** (2025), <https://api.semanticscholar.org/CorpusID:282992334>
12. Lin, H., Peng, S., Chen, J., Peng, S., Sun, J., Liu, M., Bao, H., Feng, J., Zhou, X., Kang, B.: Prompting depth anything for 4k resolution accurate metric depth estimation. In: *Proceedings of the Computer Vision and Pattern Recognition Conference*. pp. 17070–17080 (2025)
13. Mehl, L., Schmalfluss, J., Jahedi, A., Nalivayko, Y., Bruhn, A.: Spring: A high-resolution high-detail dataset and benchmark for scene flow, optical flow and stereo. In: *Proc. IEEE/CVF Conference on Computer Vision and Pattern Recognition (CVPR)* (2023)
14. Ranftl, R., Lasinger, K., Hafner, D., Schindler, K., Koltun, V.: Towards robust monocular depth estimation: Mixing datasets for zero-shot cross-dataset transfer. *IEEE Transactions on Pattern Analysis and Machine Intelligence* **44**, 1623–1637 (2019), <https://api.semanticscholar.org/CorpusID:195776274>
15. Schönberger, J.L., Zheng, E., Pollefeys, M., Frahm, J.M.: Pixelwise view selection for unstructured multi-view stereo. In: *European Conference on Computer Vision (ECCV)* (2016)
16. Schöps, T., Sattler, T., Pollefeys, M.: BAD SLAM: Bundle adjusted direct RGB-D SLAM. In: *Conference on Computer Vision and Pattern Recognition (CVPR)* (2019)
17. Tung, J., Chou, G., Cai, R., Yang, G., Zhang, K., Wetzstein, G., Hariharan, B., Snavely, N.: Megascenes: Scene-level view synthesis at scale. ArXiv **abs/2406.11819** (2024)
18. Viola, M., Qu, K., Metzger, N., Ke, B., Becker, A., Schindler, K., Obukhov, A.: Marigold-dc: Zero-shot monocular depth completion with guided diffusion. In: *Proceedings of the IEEE/CVF International Conference on Computer Vision*. pp. 5359–5370 (2025)
19. Vuong, K., Ghosh, A., Ramanan, D., Narasimhan, S., Tulsiani, S.: Aerialmegadepth: Learning aerial-ground reconstruction and view synthesis. In: *Proceedings of the IEEE/CVF Conference on Computer Vision and Pattern Recognition* (2025)

20. Wang, R., Xu, S., Dai, C., Xiang, J., Deng, Y., Tong, X., Yang, J.: Moge: Unlocking accurate monocular geometry estimation for open-domain images with optimal training supervision. In: Proceedings of the Computer Vision and Pattern Recognition Conference. pp. 5261–5271 (2025)
21. Wang, R., Xu, S., Dong, Y., Deng, Y., Xiang, J., Lv, Z., Sun, G., Tong, X., Yang, J.: Moge-2: Accurate monocular geometry with metric scale and sharp details. arXiv preprint arXiv:2507.02546 (2025), <https://arxiv.org/abs/2507.02546>
22. Wang, Y., Zhou, J., Zhu, H., Chang, W., Zhou, Y., Li, Z., Chen, J., Pang, J., Shen, C., He, T.: Pi3: Permutation-equivariant visual geometry learning. arXiv preprint arXiv:2507.13347 (2025)
23. Wang, Y., Lipson, L., Deng, J.: Sea-raft: Simple, efficient, accurate raft for optical flow. In: European Conference on Computer Vision. pp. 36–54. Springer (2024)
24. Wen, B., Trepte, M., Aribido, J., Kautz, J., Gallo, O., Birchfield, S.: Foundation-stereo: Zero-shot stereo matching. In: Proceedings of the IEEE/CVF conference on computer vision and pattern recognition. pp. 5249–5260 (2025)
25. Xiangli, Y., Cai, R., Chen, H., Byrne, J., Snavely, N.: Doppelgangers++: Improved visual disambiguation with geometric 3d features (2025)
26. Xie, E., Wang, W., Yu, Z., Anandkumar, A., Alvarez, J.M., Luo, P.: Segformer: Simple and efficient design for semantic segmentation with transformers. *Advances in neural information processing systems* **34**, 12077–12090 (2021)
27. Yang, L., Kang, B., Huang, Z., Zhao, Z., Xu, X., Feng, J., Zhao, H.: Depth anything v2. In: NeurIPS (2024)

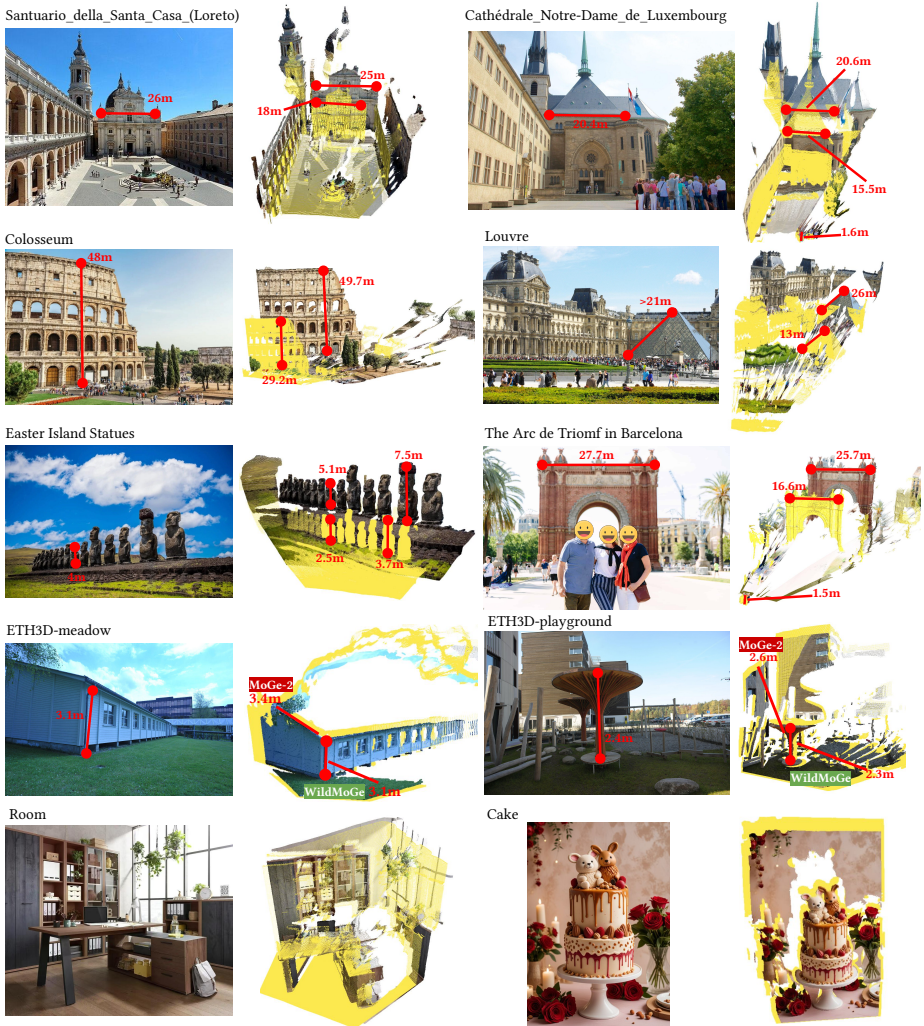


**Fig. 6: Additional visualizations of inferred scene point clouds.** Measurements annotated in the images are obtained either from maps or from ground truth. For clarity, results from MoGe-2 are shown with yellow points. The first three rows correspond to novel scenes (*i.e.* not in the training set), where MoGe-2 exhibits a scale-collapse issue and consistently predicts a smaller scale than the ground truth. The fourth row shows scenes from ETH3D: while MoGe-2 and WildMoGe predict similar scales, WildMoGe tends to be closer to the ground truth. The final row presents random images from the MoGe-2 demo, where the two models produce similar predictions.